INTERNATIONAL JOURNAL FOR NUMERICAL METHODS IN FLUIDS
Int. J. Numer. Meth. Fluids 2004; **44**:147–174 (DOI: 10.1002/fld.633)

Indirect boundary element method for unsteady linearized flow over prolate and oblate spheroids and hemispheroidal protuberances

Lisa F. Shatz*,[1,2,†]

[1]*Suffolk University, Boston, MA 02114, U.S.A.*
[2]*Boston University Hearing Research Center, Boston, MA 02115, U.S.A.*

SUMMARY

The indirect boundary element method was used to study the hydrodynamics of oscillatory viscous flow over prolate and oblate spheroids, and over hemispheroidal bodies hinged to a plate. Analytic techniques, such as spheroidal co-ordinates, method of images, and series representations, were used to make the numerical methods more efficient. A novel method for computing the hydrodynamic torque was used, since for oscillatory flow the torque cannot be computed directly from the weightings. Instead, a Green's function for torque was derived to compute the torque indirectly from the weightings. For full spheroids, the method was checked by comparing the results to exact solutions at low and high frequencies, and to results computed using the singularity method. For hemispheroids hinged to a plate, the method for low frequencies was checked by comparing the results to previous results, and to exact solutions at high frequencies. Copyright © 2004 John Wiley & Sons, Ltd.

KEY WORDS: numerical methods; boundary element method; linearized flow; hydrodynamics; spheroids; hair bundles

1. INTRODUCTION

When the acceleration forces of a fluid dominate the non-linear inertial forces in unsteady viscous flow, the hydrodynamic equations can be linearized, and the analysis becomes much more tractable. This linearization is valid for low-amplitude oscillatory behaviour such as flow produced by Brownian motion of microscopic particles and flow produced by the swimming of microscopic organisms. It is also valid for the hydrodynamics of hair bundles protruding from the sensory epithelium of inner ear organs [1], which are the object of this research. There have been previous studies of flow over protuberances for Stokes flow [2–4] and studies of Stokes flow for spheroidal shapes [5, 6], however these studies are not sufficient to understand

---

*Correspondence to: L. F. Shatz, 41 Temple Street, Suffolk University, Boston, MA 02114, U.S.A.
†E-mail: shatz@ee.suffolk.edu

Contract/grant sponsor: National Science Foundation; contract/grant number: 0099753

Received 20 May 2003
Revised 11 August 2003

hair bundle hydrodynamics since it has been shown that inertial forces can be important at auditory frequencies [1].

2. BACKGROUND

The overall goal of this research is to understand the relationship between the morphology of inner ear hair bundle structures and their functionality, in particular, how their size and shape affect their responses to stimuli of different frequencies. Hair bundles vary in shape and size among different hair cells; for instance, hair bundles of hair cells that control balance in vestibular organs that sense motion with frequencies less than one hertz, are taller (40–120 μm) than hair bundles in hearing organs that sense sound of frequencies between 20 and 20 000 Hz (0.8–30 μm) [7].

Previously the hydrodynamics of a single hair bundle, modelled as a two-dimensional flap [8] and as a three-dimensional hemispheroid [4, 9–11] were investigated. The three-dimensional hemispheroid model was analysed only in the limit of high and low frequencies. The results of the 3-D model indicated that the sensitivity of the responses of hair cells at low frequencies was mainly proportional to the cube of the heights of their hair bundles, and at high frequencies, the sensitivity of the hair cells was mainly proportional to the inverse of their heights. These results provide a reason for why hair bundle heights in vestibular organs are one to two orders of magnitude taller than hair bundles in hearing organs [9]. Since the 2-D model of hair bundle hydrodynamics that was valid for all frequencies cannot model 3-D effects, this study presents results for a 3-D model valid for all frequencies.

Professors D. Freeman and T. Weiss of M.I.T. have developed a general model that can be used to analyse the hydrodynamics of hair bundles in the inner ear [8, 12–14]. Their aim in developing this model was to make it as simple as possible by only including the features of the hair cell structure important to its hydrodynamics.

The hair bundle is stiff, and so it is represented as a rigid body. Since the hair bundle is compliantly attached to the epithelium surface, the attachment is represented as a spring-loaded hinge, and the epithelium from which the hair bundle emerges is represented as a rigid basal plate (Figure 1). The rigid body is immersed in an incompressible Newtonian fluid.

The hydrodynamics of the hair bundle motion is thought to play a key role in the frequency tuning of hair cells in the free-standing region of the alligator lizard (Figure 2), whose basilar papilla on which the hair cells lie has no tuning properties (unlike that of most other species), and whose hair bundle heights vary along its length (like that of most other species). Since the cross-section of its hair bundle is somewhat circular at its base, and since the effect of shape on the hydrodynamics is of interest, the rigid body chosen to represent a hair bundle is the hemispheroid, whose cross section is circular, and whose shape is mathematically easy to represent and to change.

The motion of the rigid body can be understood as follows. The shearing component of the motion of the basal plate rotates the body about the hinge.

This rotation is resisted by torques of fluid origin and by torques of mechanical origin that arise in the rotational stiffness of the hinged attachment.

The rigid body has two distinct modes of motion—translation and rotation. In translation, the plate is translated and the hinge is fixed to the plate, while in rotation, the rigid body is rotated about its hinge and the plate is stationary. For infinitesimally small motions, a

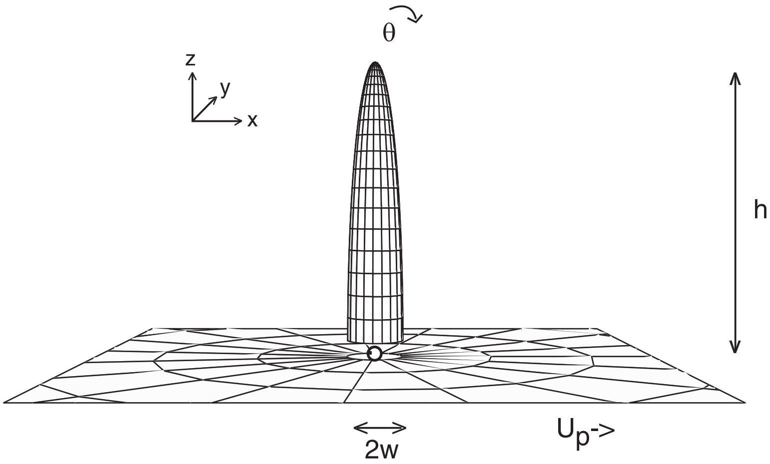

Figure 1. A prolate hemispheroid compliantly attached by a hinge to a plate. In response to the plate translating, the hemispheroid both translates and rotates about the hinge.

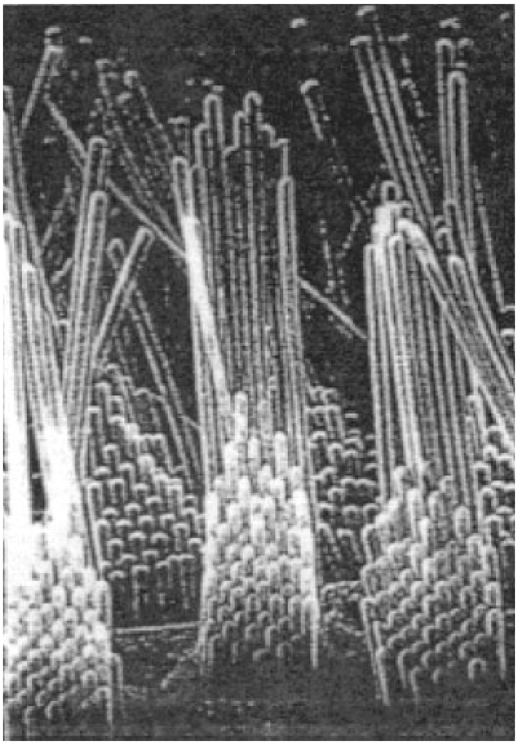

Figure 2. A scanning electromicrograph of hair bundles found in the basilar papilla of the alligator lizard. Hair bundles of three hair cells are shown in the foreground. Hair bundles are rigid and move as a unit (although that is not obvious from the micrograph). Taken by Ruth Anne Eatock.

stationary boundary approximation can be used [15] and the equations of motion can be linearized [1, 12], and so the torques due to translation of the basal plate, and rotation of the hemispheroid can be determined separately and then superposed [12].

We represent the instantaneous angular displacement of the rigid body as $\theta(t)$ which in the sinusoidal steady state is represented as $\theta(t) = \theta e^{-i\omega t}$ where θ is the complex amplitude of the angular displacement and ω is the radian frequency of oscillation. Similarly, the complex amplitude of the sinusoidal velocity of the basal plate is $U_p\hat{\mathbf{x}}$. The goal of this analysis is to determine the hair bundle sensitivity transfer function $H_\mu = \theta/U_p$ which indicates how much hair bundle deflection, and hence, how much of a signal, is obtained for a given amplitude of basilar membrane motion. H_μ depends on the hydrodynamic translational and rotational torques as well as from the mechanical torques due to the compliant hinge and the inertia of the hair bundle. Conservation of angular momentum requires that the sum of the mechanical and hydrodynamic torques equals the change in angular momentum, which can be stated in sinusoidal steady state as

$$-I\omega^2\theta = \frac{-\theta}{C} + H_i U_p + H_p U_p - i\omega\theta Z_r \tag{1}$$

where I represents the moment of inertia of the hemispheroid; C represents the compliance of the hinge; $H_i U_p$ represents a term to account for an accelerating reference frame; $H_p U_p$ represents the hydrodynamic torque due to translational motion; and $-i\omega\theta Z_r$ represents the hydrodynamic torque due to rotational motion. Therefore, from Equation (1), $H_\mu = \theta/U_p$ is represented by

$$H_\mu = \frac{H_p + H_i}{1/C - i\omega Z_r + \omega^2 I} \tag{2}$$

Since the hydrodynamic and mechanical torques are functions of hair bundle size and shape and frequency of oscillation, H_μ depends on these quantities.

In this study, the hydrodynamic torques were calculated using an indirect boundary element method (BEM). Although a direct BEM can be used, where the weightings represent real physical quantities, an indirect method is used because the Green's functions are simpler, and therefore more easily integrated.

To use the indirect method, a Green's function was derived for the hydrodynamic torque from the known Green's functions for hydrodynamic pressure and velocity.

Curvilinear co-ordinate systems, prolate and oblate spheroidal co-ordinates [16, 17] were used to discretize the domain. The use of curvilinear co-ordinates allowed for more efficient discretization because regions where the boundaries have high spatial frequencies have the smallest grid spacings. It also allowed for more efficient coding with one program describing the full range of prolate hemispheroids and one program for the full range of oblate hemispheroids. The azimuthal dependance of the weightings for spheroidal shapes has previously been determined for Stokes flow [4, 18], and the results are valid for linearized oscillatory flow too. Therefore, only a one-dimensional discretization was needed. To make the computations more efficient, truncations of infinite series representations were used when valid and the integrations were performed analytically instead of numerically. The infinite plate was approximated with a finite plate with a sufficiently large radius.

To check this method, the low frequency solutions were compared to the results of previous studies [4] and the high frequency solutions were compared to exact solutions [11]. For further comparison, this method was also applied to full spheroids, where exact solutions exist for low frequencies [5, 19] and high frequencies [5, 16, 20] and whose hydrodynamics have been shown to be similar to that of hemispheroids protruding from plates [4].

3. PROBLEM FORMULATION

A hemispheroid compliantly hinged to a plate is shown in (Figure 1). Incompressible flow is assumed, and we set the velocity and pressure equal to $\mathbf{U}=\mathbf{u}\exp(-\mathrm{i}\omega t)$, and $P=p\exp(-\mathrm{i}\omega t)$. Therefore, conservation of momentum and conservation of mass are described, respectively, by [21]

$$-\mathrm{i}\omega\rho\mathbf{u}+\rho(\mathbf{u}\cdot\nabla)\mathbf{u}=-\nabla P+\mu\nabla^2\mathbf{u} \tag{3}$$

and

$$\nabla\cdot\mathbf{u}=0 \tag{4}$$

It has been shown that for physiologically relevant parameters, the fluid is incompressible and that the convective non-linearity term, $\rho(\mathbf{u}\cdot\nabla)\mathbf{u}$, is four orders of magnitude less than the first term, $-\mathrm{i}\omega\rho\mathbf{u}$ [1], and therefore Equation (3) can be linearized,

$$-\mathrm{i}\omega\rho\mathbf{u}=-\nabla P+\mu\nabla^2\mathbf{u} \tag{5}$$

We assume the plate translates in its plane with velocity $\mathbf{U_p}=U_\mathrm{p}\exp(-\mathrm{i}\omega t)\hat{\mathbf{x}}$. In response to the plate translating, the hemispheroid translates and rotates infinitesimally with angle $\boldsymbol{\theta}=\theta\exp(-\mathrm{i}\omega t)\hat{\boldsymbol{\theta}}$. The boundary condition far from the hemispheroid is the velocity due to a plate translating with no hemispheroid present $\mathbf{u}=U_\mathrm{p}\exp\left(-z\sqrt{-\mathrm{i}\omega\rho/\mu}\right)\hat{\mathbf{x}}$ [22]. The boundary conditions along the hemispheroid, plate, and at infinity, are thus given respectively by

$$\begin{aligned}\mathbf{u}(r=r')&=U_\mathrm{p}\hat{\mathbf{x}}-\mathrm{i}\omega\theta(z\hat{\mathbf{x}}-x\hat{\mathbf{z}})\\ u(z=0)&=U_\mathrm{p}\hat{\mathbf{x}}\\ \mathbf{u}(r'\to\infty)&=U_\mathrm{p}\exp\left(-z\sqrt{-\mathrm{i}\omega\rho}/\mu\right)\hat{\mathbf{x}}\end{aligned} \tag{6}$$

where r' denotes the surface of the hemispheroid. The torque on a hemispheroid is given by

$$\mathbf{T}=\int_S\mathbf{r}\cdot\mathbf{dF} \tag{7}$$

where $\mathbf{r}$ represents a vector to a point on the surface S of the hemispheroid and,

$$\mathbf{dF}=-P\mathbf{dS}+\mu(\mathbf{dS}\cdot\nabla)\mathbf{u}+\mu\nabla(\mathbf{dS}\cdot\mathbf{u}) \tag{8}$$

where $\mathbf{dS}$ is in the normal direction to the surface. Due to the reflection symmetry about the x–z plane, the torque has only a y component.

The computations are best performed in a reference frame shifted by $U_\mathrm{p}\exp\left(-z\sqrt{-\mathrm{i}\omega\rho/\mu}\right)\hat{\mathbf{x}}$ so that the fluid is stationary at infinity, allowing the use of Green's functions which vanish at infinity. For this frame of reference, the equations of motion remain the same while the boundary conditions can be expressed as

$$\mathbf{u}(r=r') = U_{\rm p}(1 - \exp\left(-z\sqrt{-{\rm i}\omega\rho/\mu}\right))\hat{\mathbf{x}} - {\rm i}\omega\theta(z\hat{\mathbf{x}} - x\hat{\mathbf{z}})$$

$$\mathbf{u}(z=0) = 0$$

$$\mathbf{u}(r' \to \infty) = 0$$

The pressure term needs no modification since the addition of $U_{\rm p} \exp\left(-z\sqrt{-{\rm i}\omega\rho/\mu}\right)\hat{\mathbf{x}}$ to the velocity does not change Equation (5) because

$$-{\rm i}\omega\rho U_{\rm p} \exp\left(-z\sqrt{-{\rm i}\omega\rho/\mu}\right)\hat{\mathbf{x}} - \mu\nabla^2(U_{\rm p} \exp\left(-z\sqrt{-{\rm i}\omega\rho/\mu}\right)\hat{\mathbf{x}}) = 0$$

The torque however is changed by an amount found by substituting $\mathbf{u} = U_{\rm p} \exp\left(-z\sqrt{-{\rm i}\omega\rho/\mu}\right)\hat{\mathbf{x}}$ into Equations (7) and (8). This shift in torque will be given in Section 6.

Since the equations of motion are linear, superposition can be used to separately solve Equations (5) and (4) for the plate translating with no rotation ($\theta = 0$), and for the hemispheroid rotating with no plate motion ($U_{\rm p} = 0$). The boundary conditions for translational motion can be written as

$$\mathbf{u}(r=r') = U_{\rm p}\left(1 - \exp\left(-z\sqrt{-{\rm i}\omega\rho/\mu}\right)\right)\hat{\mathbf{x}}$$

$$\mathbf{u}(z=0) = 0$$

and for rotational motion, the boundary conditions are

$$\mathbf{u}(r=r') = -{\rm i}\omega\theta(z\hat{\mathbf{x}} - x\hat{\mathbf{z}})$$

$$\mathbf{u}(z=0) = 0$$

We will solve for the hydrodynamic quantities using spheroidal co-ordinates and an indirect BEM method.

4. SPHEROIDAL CO-ORDINATES

We chose to use spheroidal co-ordinates where the hemispheroid and plate are co-ordinate surfaces. Spheroidal co-ordinates, represented by ξ, η, ϕ, are similar to spherical co-ordinates, represented by r, θ and ϕ. As with a sphere, a cross-section of a spheroid parallel to the x–y lane has the shape of a circle; however, a cross-section of a spheroid perpendicular to the x–y plane has the shape of an ellipse.

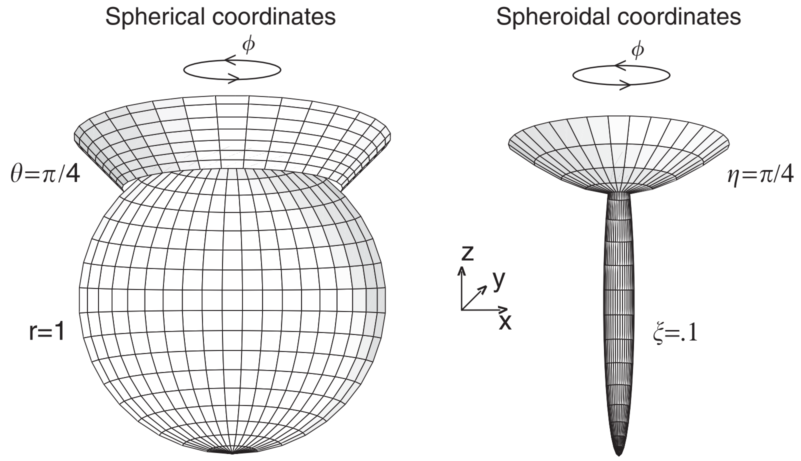

Figure 3. Left: A surface of constant r describes a sphere and a surface of constant θ describes a half-cone in spherical co-ordinates. Right: A surface of constant ξ describes a spheroid and a surface of constant η describes a hyperboloid in spheroidal co-ordinates.

There are two types of spheroids—prolate and oblate. For prolate spheroids, the heights of the cross-sectional ellipses are larger than the widths; for oblate spheroids, the converse is true. Figure 3 illustrates the similarities and differences between spheroidal and spherical co-ordinates. Prolate spheroidal co-ordinates are defined by

$$\begin{aligned} x &= L\sinh\xi\sin\eta\cos\phi \\ y &= L\sinh\xi\sin\eta\sin\phi \\ z &= L\cosh\xi\cos\eta \end{aligned} \tag{9}$$

Let $\xi=\xi_0$ represent the surface of a spheroid. For a prolate spheroid, the half-height h and half-width w are represented by $h=L\cosh\xi_0$, $w=L\sinh\xi_0$. Oblate spheroidal co-ordinates can be obtained from Equation (9) by replacing $\cosh\xi$ with $i\sinh\xi$ and L with $-iL$.

5. HEMISPHEROID ON A PLATE

To describe a hemispheroid, we restrict η to range from zero to $\pi/2$. The tip of the hemispheroid is at $\eta=0$; the base is at $\eta=\pi/2$. Figure 4 illustrates the hemispheroid on a plate in rectangular co-ordinates and in spheroidal co-ordinates.

6. TORQUE IN FRAME OF REFERENCE FOR TRANSLATIONAL MOTION

The magnitude of the hydrodynamic torque due to translational motion of the plate can be represented by

$$T = T_{uc} - T_{\rm s}$$

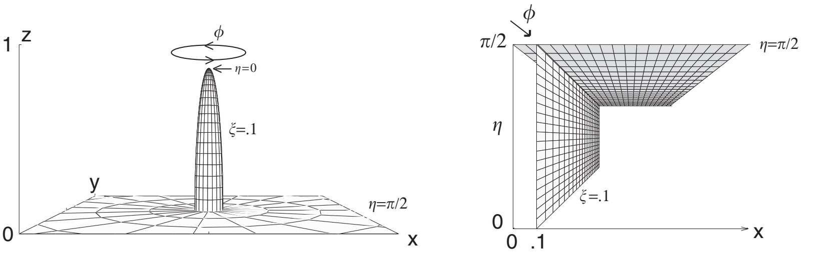

Figure 4. The hemispheroid on a plate is defined by a surface of constant ξ and the surface $\eta = \pi/2$. The hemispheroid and plate in rectangular co-ordinates (left panel) transform to orthogonal planes in spheroidal co-ordinates.

where T_{uc} is the torque that will be computed numerically, and T_s is the shift in torque due to change of reference frame. T_s can be found by integrating Equation (7) on the surface of the hemispheroid, with $\mathbf{u} = U_\mathrm{p} \exp\left(-z\sqrt{-\mathrm{i}\omega\rho/\mu}\right)\hat{\mathbf{x}}$. Let $\lambda = \sqrt{-\mathrm{i}\omega\rho/\mu}h$. The portion of the torque due to the reference frame shift is

$$T_\mathrm{s} = \pi \frac{w^2}{\lambda^2}\left(2 + \lambda^2 - 2\mathrm{e}^{-\lambda}(1 + \lambda + \lambda^2)\right) \tag{10}$$

We consider hemispheroids of the same height. Since T_s is proportional to w^2, the shift in torque due do a change in reference frame is more significant for oblate shapes than prolate shapes.

7. BOUNDARY ELEMENT METHODS

The BEM is a numerical approximation of the boundary integral or singularity method (BIM), which represents the solutions to a homogeneous linear differential equation with specified boundary conditions as a weighted integral of Green's functions,

$$\begin{aligned} u_i(\lambda, \mathbf{r}) = \int_{s'} (&w_x(\lambda, \eta', \phi')G_{uxi}(\lambda, \mathbf{r} - \mathbf{r}') + w_y(\lambda, \eta', \phi')G_{uyi}(\lambda, \mathbf{r} - \mathbf{r}') \\ &+ w_z(\lambda, \eta', \phi')G_{uzi}(\lambda, \mathbf{r} - \mathbf{r}'))\,\mathrm{d}S' \end{aligned} \tag{11}$$

where $u_i(\mathbf{r})$ represents the ith component of fluid velocity, $w_j(\lambda, \eta', \phi')$ represents the weighting of the jth component of a velocity stokeslet, and $G_{uji}(\lambda, \mathbf{r} - \mathbf{r}')$ represents the jth component of a velocity stokeslet due to an impulse in the ith direction.

For Stokes flow, both the force and torque can be computed directly form the weightings of the Green's functions. For linearized oscillatory flow, the force can still be found directly from the weightings [6] although the torque cannot. However, we can compute the torque from the weightings by using a Green's function for torque, which will be derived in a subsequent section.

7.1. *Green's functions for linearized oscillating flow*

In the manner of [6], let us write Equation (5) with non-dimensional variables,

$$\lambda^2\mathbf{u} = -\nabla P + \nabla^2\mathbf{u}$$

Equation (4) is still satisfied with non-dimensional variables. The simplest Green's functions of Equations (5) and (4) are known as oscillating stokeslets [6]. $\mathbf{G}_{ui}(\lambda, \mathbf{r})$ the ith component of the velocity stokeslet due to a three dimensional impulse at the origin can be expressed as

$$\mathbf{G}_{\mathbf{u}i}(\lambda, \mathbf{r}) = \frac{1}{8\pi\mu}\left(A\,\frac{\hat{\mathbf{x}}_i}{r} + B\,\frac{x_i^2\hat{\mathbf{x}}_i + x_i x_j\hat{\mathbf{x}}_j + x_i x_k\hat{\mathbf{x}}_k}{r^3}\right)$$

where

$$A = 2\mathrm{e}^{-\lambda r}\left(1 + \frac{1}{\lambda r} + \frac{1}{(\lambda r)^2}\right) - \frac{2}{(\lambda r)^2}$$

$$B = -2\mathrm{e}^{-\lambda r}\left(1 + \frac{3}{\lambda r} + \frac{3}{(\lambda r)^2}\right) + \frac{6}{(\lambda r)^2}$$

The pressure oscillating stokeslet is the same as the stokeslet for Stokes flow and can be expressed as

$$G_{pi}(\mathbf{r}) = \frac{1}{4\pi}\,\frac{x_i\hat{\mathbf{x}}_i}{r^3}$$

The stokeslets for impulses not on the origin can be expressed by substituting $r - r'$ for r. Note that although the stokeslet is singular at $r = r'$, the singularity in integrable, and numerical integration can be performed.

7.2. $\boldsymbol{\varphi}'$ *dependency of the stokeslet weightings*

The $\boldsymbol{\varphi}'$ dependency of the stokeslet weightings have been previously derived for Stokes flow [4], and the analysis is equally valid for oscillating flow. We therefore represent the stokeslets weightings as

$$w_x(\lambda, \eta', \phi') = w_x'(\lambda, \eta') + w_{xy}'(\lambda, \eta')\cos^2\phi'$$

$$w_y(\lambda, \eta', \phi') = w_{xy}'(\lambda, \eta')\sin\phi'\cos\phi'$$

$$w_z(\lambda, \eta', \phi') = w_z'(\lambda, \eta')\cos\phi'$$

where the $w_i'(\lambda, \eta')$'s are to be determined numerically.

7.3. *Analytic integration of* $\boldsymbol{\varphi}'$ *dependence*

The stokeslet weightings can be integrated analytically with respect to ϕ' by expressing the stokelets with their weightings in spheroidal co-ordinates. The result is an infinite series, which converges after the first three terms when λ is not too large, and the collocation point is not near the stokeslet. The analytic integration is discussed in more detail in Appendix A. The integrated stokeslet was used when the ratio of the third term to the second term of the series was less than 0.001.

7.4. Use of image stokeslet

For full spheroids an image stokeslet can be used because of the symmetry about the x–y plane. The image stokeslets are negative stokeslets in $\hat{\mathbf{x}}$ and $\hat{\mathbf{y}}$ and positive in $\hat{\mathbf{z}}$ for the case of rotational motion. For hemispheroids on a plate, the numerical analysis was made more rapidly convergent with the use of a negative image stokeslet in each direction. Since the boundary conditions along the plate cannot be fully satisfied with the use of image stokeslets, it was also necessary to put stokeslets along the plate.

7.5. Numerical method to compute the η' dependence of weights

An arc at $\phi=\pi/4$ was discretized into n sections from $\eta=0$ to π for a full spheroid and $\eta=\pi/2$ for a hemispheroid, with each section having the same range of $\pi/2n$, and the weights represented as constant in each section (Figure 5). For the full spheroid, only the boundary conditions along the arc were used to determine the weightings. For the hemispheroid on a plate, a line segment along the plate was discretized to $\xi=\xi_{\mathrm{ab}}$ with $n/2$ sections. ξ_{ab}, the limit of the artificial boundary, was chosen large enough such that increasing its value has no significant effect on the results. A collocation point was chosen as the midpoint of each section. For full spheroids, since there are three weightings for each section, and three components of boundary velocities, there are $3n$ boundary equations for $3n$ unknown weightings. For hemispheroids on plates, there are $3n+3n/2$ boundary equations for $3n+3n/2$ unknown weightings.

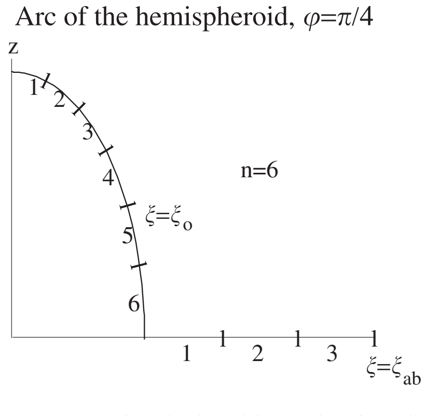

Figure 5. The discretation arc for a hemispheroid. A circular plate extends out to $\xi=\xi_{\mathrm{ab}}$, the artificial boundary. Here there are $n=6$ sections, and the collocation point is chosen as the midpoint of each section.

We can therefore represent Equation (11) for full spheroids as

$$u_i(\lambda,\mathbf{r}) = \sum_k \int_{\eta',k} [w'_{xk}(\lambda,\eta')(G'_{uxi0k}(\lambda,\eta',\mathbf{r}) - G'_{uxi0k}(\lambda,\pi-\eta',\mathbf{r}))$$

$$+ w'_{xyk}(\lambda,\eta')(G'_{uxi2k}(\lambda,\mathbf{r},\eta') - G'_{uxi2k}(\lambda,\mathbf{r},\pi-\eta') + G'_{uyik}(\lambda,\mathbf{r},\eta') - G'_{uyik}(\lambda,\mathbf{r},\pi-\eta'))$$

$$+ w'_{zk}(\lambda,\eta')(G'_{uzik}(\lambda,\mathbf{r},\eta') + G'_{uzik}(\lambda,\mathbf{r},\pi-\eta'))]$$

where $G'_{ujik}(\lambda,\mathbf{r},\eta')$ represents the stokeslet after integrating over ϕ'. For hemispheroids on plates Equation (11) is represented as

$$u_i(\lambda,\mathbf{r}) = \sum_k \int_{\eta',k} [w'_{xk}(\lambda,\eta')(G'_{uxi0k}(\lambda,\eta',\mathbf{r}) - G'_{uxi0k}(\lambda,\pi-\eta',\mathbf{r}))$$

$$+ w'_{xyk}(\lambda,\eta')(G'_{uxi2k}(\lambda,\mathbf{r},\eta') - G'_{uxi2k}(\lambda,\mathbf{r},\pi-\eta') + G'_{uyik}(\lambda,\mathbf{r},\eta') - G'_{uyik}(\lambda,\mathbf{r},\pi-\eta'))$$

$$+ w'_{zk}(\lambda,\eta')(G'_{uzik}(\lambda,\mathbf{r},\eta') - G'_{uzik}(\lambda,\mathbf{r},\pi-\eta'))]$$

$$+ \sum_l \int_{\xi',l} w'_{xl}(\lambda,\xi')G'_{uxi0l}(\lambda,\xi',\mathbf{r}) + w'_{xyl}(\lambda,\xi')(G'_{uxi2l}(\lambda,\mathbf{r},\xi')$$

$$+ G'_{uyil}(\lambda,\mathbf{r},\xi')) + w'_{zl}(\lambda,\xi')G'_{uzil}(\lambda,\mathbf{r},\xi')$$

The analysis was performed using *Mathematica* [23].

7.6. Derivation of torque stokeslet

Once the weightings have been determined, the torque can be found using torque stokeslets. The torque stokeslet can be derived from the velocity and pressure stokeslets by substituting $\mathbf{u} = G_{ui}(\mathbf{r})$ and $P = G_{pi}(\mathbf{r})$ into Equations (7) and (8). The result can be integrated analytically with respect to ϕ, although numerical integration is necessary for the other directions. For full spheroids, the torque can be expressed as

$$T(\lambda,\mathbf{r}) = \sum_k \int_S \int_{\eta',k} [w'_{xk}(\lambda,\eta')(T'_{uxi0k}(\lambda,\eta',\mathbf{r}) - T'_{uxi0k}(\lambda,\pi-\eta',\mathbf{r}))$$

$$+ w'_{xyk}(\lambda,\eta')(T'_{uxi2k}(\lambda,\mathbf{r},\eta') - T'_{uxi2k}(\lambda,\mathbf{r},\pi-\eta') + T'_{uyik}(\lambda,\mathbf{r},\eta') - T'_{uyik}(\lambda,\mathbf{r},\pi-\eta'))$$

$$+ w'_{zk}(\lambda,\eta')(T'_{uzik}(\lambda,\mathbf{r},\eta') + T'_{uzik}(\lambda,\mathbf{r},\pi-\eta'))]$$

where $T'_{ujik}(\lambda,\mathbf{r},\eta')$ represents the integrated torque stokeslet with respect to ϕ'. Appendix B contains the integrated torque stokeslets. For hemispheroids on plates, additional terms are required to account for the stokeslets on the plate,

$$\begin{aligned}
T(\lambda,\mathbf{r}) = \sum_k \int_S \int_{\eta',k} & [w'_{xk}(\lambda,\eta')(T'_{uxi0k}(\lambda,\eta',\mathbf{r}) - T'_{uxi0k}(\lambda,\pi-\eta',\mathbf{r})) \\
& + w'_{xyk}(\lambda,\eta')(T'_{uxi2k}(\lambda,\mathbf{r},\eta') - T'_{uxi2k}(\lambda,\mathbf{r},\pi-\eta') + T'_{uyik}(\lambda,\mathbf{r},\eta') - T'_{uyik}(\lambda,\mathbf{r},\pi-\eta')) \\
& + w'_{zk}(\lambda,\eta')(T'_{uzik}(\lambda,\mathbf{r},\eta') - T'_{uzik}(\lambda,\mathbf{r},\pi-\eta'))] \\
& + \sum_l \int_S \int_{\xi',l} [w'_{xl}(\lambda,\xi')T'_{uxi0l}(\lambda,\xi',\mathbf{r}) \\
& + w'_{xyl}(\lambda,\xi')(T'_{uxi2l}(\lambda,\mathbf{r},\xi') + T'_{uyil}(\lambda,\mathbf{r},\xi')) + w'_{zl}(\lambda,\xi')T'_{uzil}(\lambda,\mathbf{r},\xi')]
\end{aligned}$$

7.7. Simplifications at low and high frequencies

At low frequencies as $\lambda - > 0$, the simpler Stokes flow equations can be used to represent the hydrodynamics [4], and at high frequencies, as $\lambda - > \infty$, Laplace's equation can be used [11]. Exact solutions at low and high frequencies for full spheroids have been derived [4, 5, 20], and at high frequencies for hemispheroids on plates [11, 16]. There have been previous numerical results for hemispheroids on plates for Stokes flow [4, 18]. All these previous results will be used as a check on the solutions.

8. RESULTS FOR FULL SPHEROIDS

Excellent results were obtained for full spheroids undergoing rotational motion. Figure 6 illustrates the BEM results for torque as a function of λ as well as the results obtained using the singularity method [24]. Slight differences are attributed to numerical errors. The results match exact solutions for small λ, and approach exact solutions for high λ for the full range of shapes. The results are shown for the highest λ that gave a good match to the boundary velocities off the collocation points.

9. RESULTS FOR HEMISPHEROIDS ON PLATES

Very good results have been obtained for hemispheroids on plates for prolate shapes, and good results have been obtained for oblate shapes.

9.1. Low frequency solution

Figure 7 illustrates the results for low frequencies for the full range of shapes for rotational motion and translational motion. Also shown are the results of other studies [4, 18]. There is a noticeable difference in the results for oblate hemispheroids. Figure 8 illustrates the error in boundary conditions off the collocation points along the curve $\phi = \pi/4$ for a thin prolate

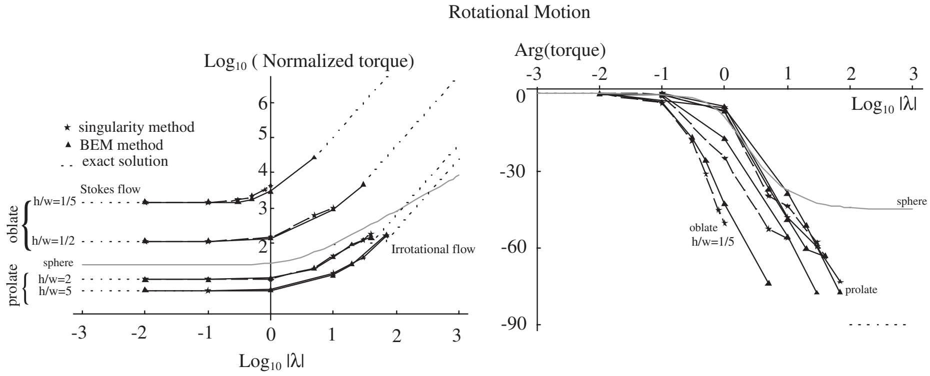

Figure 6. A comparison of the torque normalized by $(-i\omega\theta)$ for a full prolate and oblate spheroids of the same height computed using the indirect BEM method (solid lines) and the singularity method (dashed lines) for the full range of shapes. A ratio of height to half-width of $h/w = 5$ or $1/5$ corresponds to $\xi_0 = 0.2$ and $h/w = 2$ or $1/2$ corresponds to $\xi_0 = 0.549$. The results closely match, and approach exact solutions at high and low frequencies. Also shown is the exact solution for a sphere whose high frequency behaviour differs from that of the other shapes.

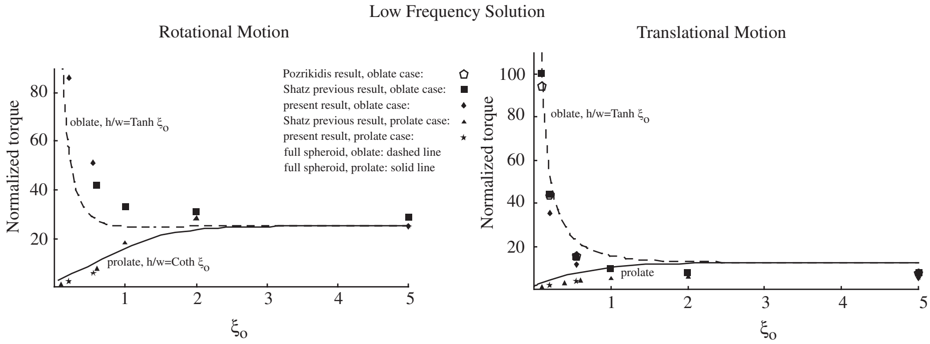

Figure 7. The low frequency torques for the full range of shapes for rotational (normalized by $-i\omega\theta$) and translational motion (normalized by $U_p\lambda$) for hemispheroids of the same height. For oblate hemispheroids, as $\xi_0 -> 0$, the width approaches infinity and so the torque approaches infinity. Results of other studies [18, 4] are also shown. The differences in the results for prolate hemispheroids are small. Larger differences are evident for wider hemispheroids.

hemispheroid and a wide oblate hemispheroid for $n = 12$. It is clear that for oblate shapes, the boundary conditions were difficult to represent along the plate and therefore some error is expected in the results. While the errors along the boundaries were smaller for $n = 12$, than for $n = 8$, increasing n to 16 or 20 did not significantly change the results. To more accurately represent the torque of oblate hemispheroids, a linear fit of the torque as a function of $1/n$ for $n = 8$ and 12 was made, and used to extrapolate the results. Thus we fit $T_{uc} = \text{torque0} + \text{torque1} * 1/n$, and the constant term, torque0, was used to estimate the torque.

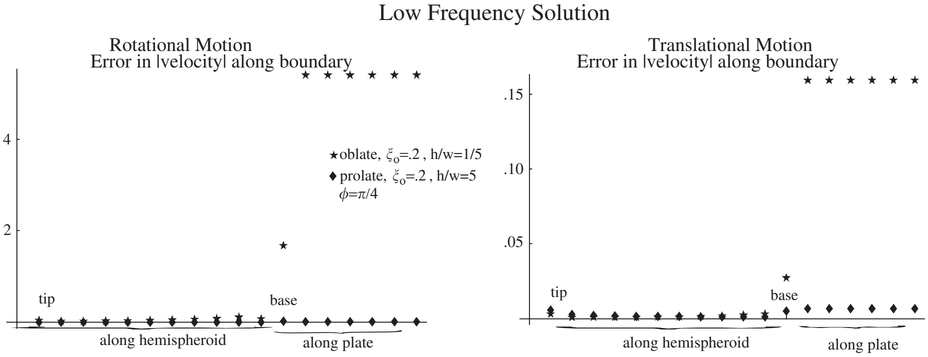

Figure 8. The error in boundary velocities for a thin prolate hemispheroid and a wide oblate hemispheroid for rotational normalized by $-\mathrm{i}\omega\theta$ (left) and translational motion normalized by $U_{\mathrm{p}}\lambda$ (right). The error along the plate is pronounced for the wide oblate hemispheroid.

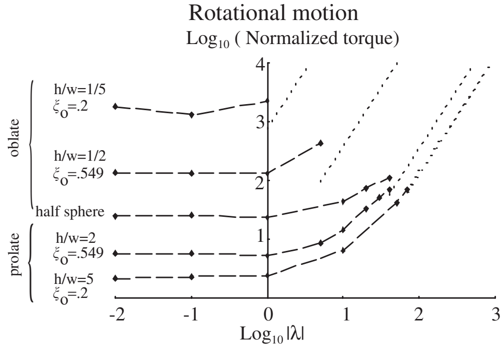

Figure 9. The magnitude of the torque normalized by $-\mathrm{i}\omega\theta$ for hemispheroids of the same height on plates for shapes ranging from thin, pencil-like to flat, disk-like for rotational motion. The dotted lines represent exact solutions for high frequencies. The high frequency torque for a half sphere on a plate is zero.

9.2. Rotational motion

The magnitude and phase for rotational motion for hemispheroids on plates whose shape ranges from thin pencil-like shapes to flat disks are shown in Figures 9 and 10 respectively. The results are similar to those of the full spheroid in rotational motion (Figure 6), although the range in λ is not as high for the oblate shapes because of the greater difficulty in matching the boundary conditions along the plate. Figure 11 illustrates the two cases on the same graph. For thin, prolate shapes, the torque for a hemispheroid on a plate is half that of a full spheroid, which is what is expected if the effect of the plate is not significant. As the shape gets wider, the torque for a hemispheroid on a plate becomes more than half that of a full spheroid. This result makes sense since the plate restricts the flow of the fluid around the hemispheroid, and therefore, the torque on the hemispheroid is greater where the effects of the plate are greater, i.e., for oblate hemispheroids. This result seems to be true throughout the frequency

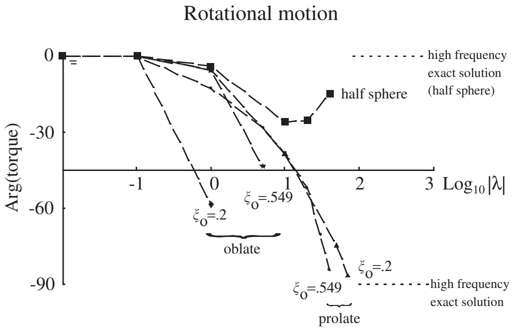

Figure 10. The argument of the torque for hemispheroids of the same height on plates for rotational motion. The argument goes from zero degrees at low frequencies to $-90°$ at high frequencies (except for the half sphere, whose torque is zero at high frequencies). A ratio of height to half-width of $h/w = 5$ or $1/5$ corresponds to $\xi_0 = 0.2$ and $h/w = 2$ or $1/2$ corresponds to $\xi_0 = 0.549$.

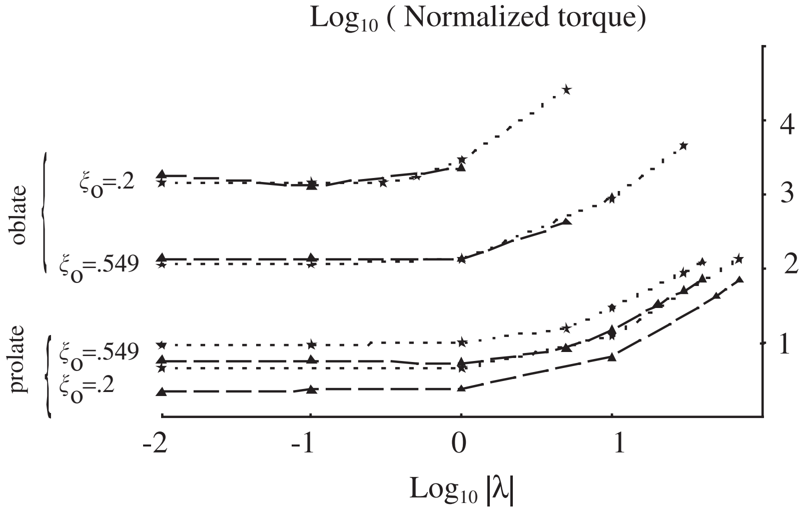

Figure 11. A comparison between the magnitude of the torque of a hemispheroid on a plate (dashed lines) and a full spheroid (dotted lines) for rotational motion. For thin, prolate shapes the results differ by a factor of 2. For wider shapes, the factor is a little more than 1. (A ratio of height to half-width of $h/w = 5$ or $1/5$ corresponds to $\xi_0 = 0.2$ and $h/w = 2$ or $1/2$ corresponds to $\xi_0 = 0.549$.)

range and Figure 12 illustrates the ratio of the torque of the full spheroid to the torque of the hemispheroid on a plate at high frequencies, for which there are exact solutions [11].

9.3. Translational motion

The magnitude (Figure 13) and phase (Figure 14) for T_{uc} for the full range of shapes are similar to the results of rotational motion at high frequencies, but are not constant with respect

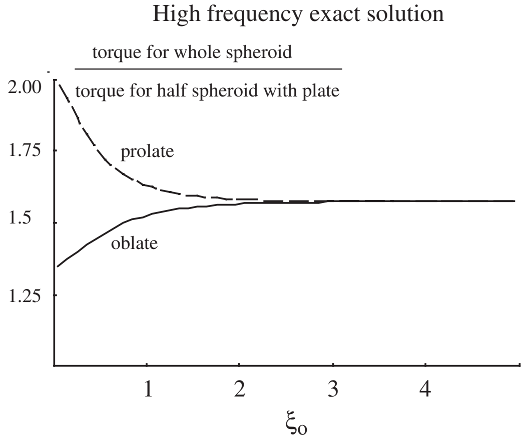

Figure 12. The ratio for rotational motion of torque of the full spheroid to torque of the hemispheroid for high frequencies.

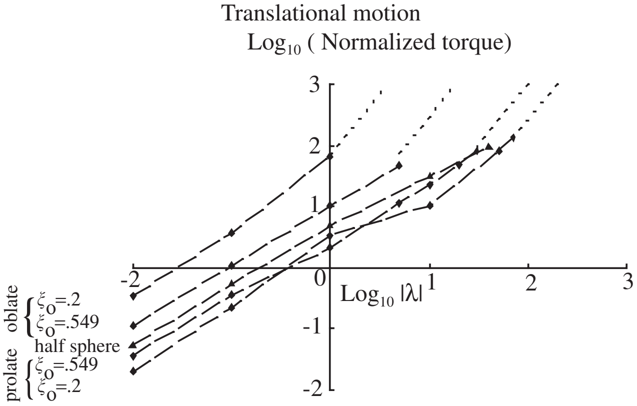

Figure 13. The magnitude of T_{uc}, the numerical result, normalized by U_p for hemispheroids of the same height on plates for shapes ranging from thin, pencil-like to flat, disk-like for translational motion. The dotted lines represent exact solutions for high frequencies. The high frequency T_{uc} for a hemisphere goes to zero so therefore it is not shown. (A ratio of height to half-width of $h/w = 5$ or 1/5 corresponds to $\xi_0 = 0.2$ and $h/w = 2$ or 1/2 corresponds to $\xi_0 = 0.549$.)

to λ at low frequencies since the boundary velocity along the hemispheroid varies with λ,

$$\mathbf{u}(r = r') = U_{\mathrm{p}}\left(1 - \exp\left(-z\sqrt{-\mathrm{i}\omega\rho/\mu}\right)\right)\hat{\mathbf{x}} = U_{\mathrm{p}}(1 - \exp(-z\lambda/h)) \approx U_{\mathrm{p}} z\lambda/h$$

The results approach the high frequency exact results for large λ.

The magnitude and phase for T_s for the full range of shapes are shown in Figure 15 and are plotted with the results for T_{uc} in Figure 16. For prolate hemispheroids, T_{uc} is significantly larger than T_s for all frequencies, so that the torque $T \approx T_{uc}$. For oblate hemispheroids $T_s > T_{uc}$

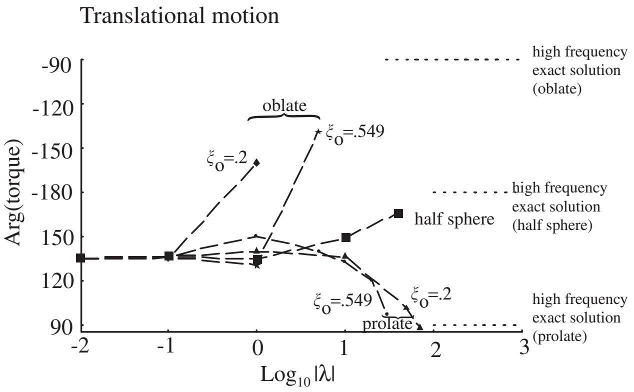

Figure 14. The argument of T_{uc} for hemispheroids of the same height on plates for translational motion. The argument goes from 135° at low frequencies to 90° at high frequencies for prolate hemispheroids, and to $-90°$ for oblate hemispheroids. (A ratio of height to half-width of $h/w = 5$ or $1/5$ corresponds to $\xi_0 = 0.2$ and $h/w = 2$ or $1/2$ corresponds to $\xi_0 = 0.549$.)

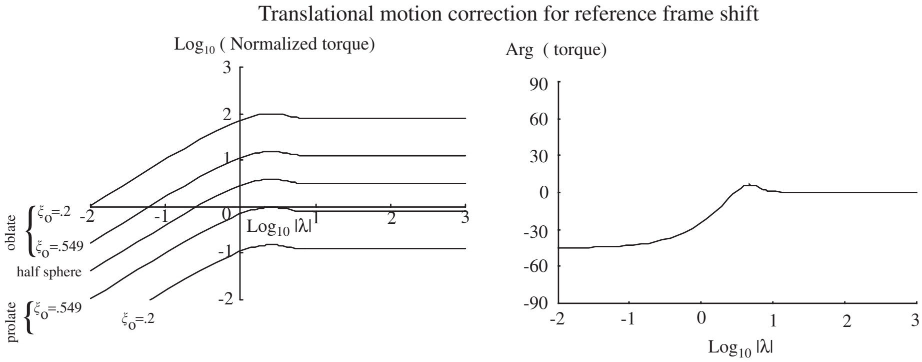

Figure 15. The torque T_s due to a shift in reference frame normalized by U_p. Since T_s is proportional to the square of the width of hemispheroid, it is greater for oblate hemispheroids.

for low frequencies, and for hemispheres $T_s \approx T_{uc}$ for low frequencies, so both terms must be used to represent the torque. Figures 17 and 18 illustrate the torque with both terms included.

10. COMPARING THE MODEL'S PREDICTIONS FOR THE HAIR BUNDLE SENSITIVITY TRANSFER FUNCTION $\mathbf{H}_\mu$ TO MEASUREMENTS OF $\mathbf{H}_\mu$ IN THE ALLIGATOR LIZARD

The results for the rotational torque T_r and the translational torque T_t were used to determine H_μ (Equation (2)) with $H_p = T_t/U_p$, and $Z_r = T_r/-I\omega\theta$. The effect of mass was found to be small and therefore the hair bundle's inertia I and the term that accounts for an accelerating reference frame H_i, were set to zero. Figure 19 illustrates the model's predictions

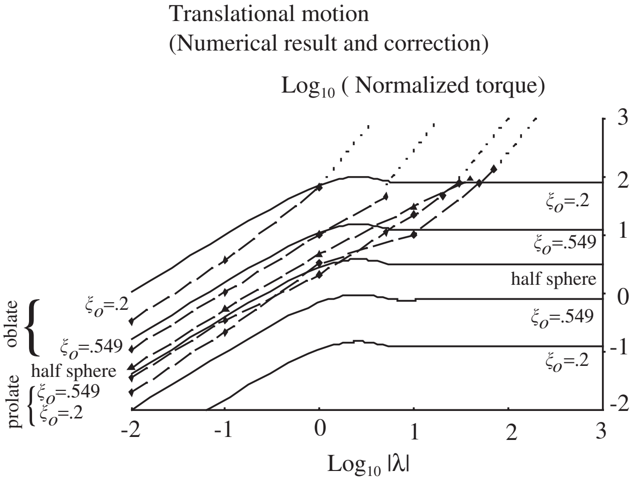

Figure 16. The numerical result, $|T_{uc}|$ (dashed), shown with $|T_s|$. At all frequencies, $|T_s|$ is smaller than $|T_{uc}|$ for thin, prolate hemispheroids. For wide oblate shapes $|T_s|$ is larger than $|T_{uc}|$ for low frequencies. The dotted lines represent exact results for the high frequency solution.

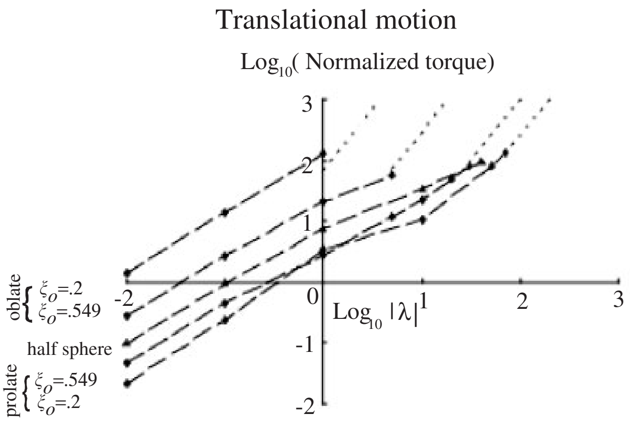

Figure 17. The magnitude of the torque for translational motion, $T_{uc} - T_s$.

and compares them with measurements taken from the basilar papilla of the alligator lizard [24]. The compliance was chosen to have a physiologically relevant value of 75 rad/N-pm (although the results matched the measurements for a wide range of compliances, all within the physiologically relevant range). An excellent match with the measurements is obtained for the prolate hemispheroid with $h/w = 2$ which makes sense considering the shapes of the hair bundles shown in Figure 2 and described in Reference [25]. A very good match is obtained for the prolate hemispheroid with $h/w = 5$. The more oblate the hemispheroid, the worse is the match. Therefore we can conclude that hydrodynamics does play a role in hair bundle motion.

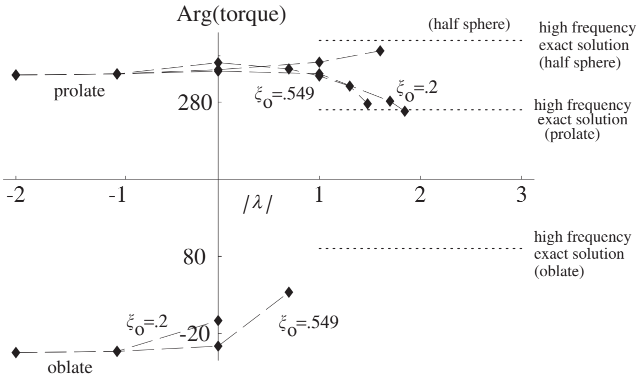

Figure 18. The argument of the torque for translational motion, $T_{uc} - T_S$.

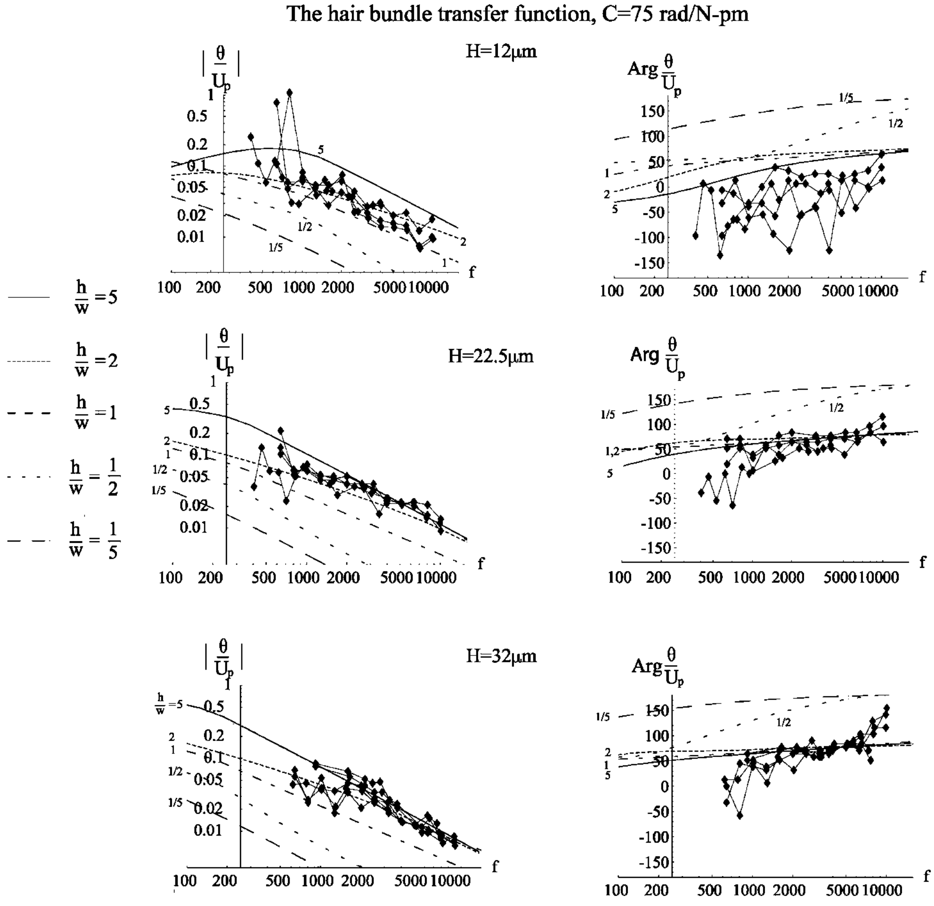

Figure 19. The hair bundle sensitivity transfer function for $C = 75$ rad/N-pm compared with measurements taken from the hair bundles of the basilar papilla of the alligator lizard. The model's predictions match the data for prolate hemispheroids, but not for oblate hemispheroids.

11. CONCLUSION

The hydrodynamic torque for prolate and oblate spheroids in infinitesimal, rotational oscillatory motion, and the hydrodynamic torques for prolate and oblate hemispheroids compliantly hinged to plates, that oscillate infinitesimally, have been computed for all frequencies using the indirect boundary element method with analytic techniques such as spheroidal co-ordinates, method of images, and series representations. A Green's function for torque was derived which was used with the stokeslet weightings to obtain the torques. For full spheroids, the results match exact solutions at low and high frequencies, and match the results of a singularity method. For hemispheroids on plates, the results match previous results at low frequencies, and approach the exact high frequency results. An excellent match is obtained for the model's predictions of the hair bundle sensitivity transfer function, and measurements of the function taken from the basilar papilla of the alligator lizard for a hair bundle represented by a hemispheroid with physiologically relevant shape.

APPENDIX A: ANALYTIC INTEGRATION OF THE OSCILLATING STOKESLETS

To perform the analytic integration of the weighted stokeslets in the $\hat{\boldsymbol{\varphi}}$ direction, we represent $|\mathbf{r}-\mathbf{r}'|$ as $|\mathbf{r}-\mathbf{r}'| = a - b\cos\phi''$, where a and b are functions of L, ξ, ξ', η, η', and $\phi'' = \phi - \phi'$.

The terms of the oscillating stokeslets that are not easily integrable with respect to ϕ'' are of the form

$$\int_0^{2\pi} (k_1 \sin^r \phi'' + k_2 \cos^m \phi'') \frac{\mathrm{e}^{-\lambda\sqrt{a-b\cos\phi''}}}{\sqrt{a-b\cos\phi''}^n} \, \mathrm{d}\phi''$$

where m, n and r are integers, with r odd. For the $k_1 \sin^r \phi''$ terms, the integral is 0 so that the terms are of the form

$$\int_0^{2\pi} k_2 \cos^m \phi'' \frac{\mathrm{e}^{-\lambda\sqrt{a-b\cos\phi''}}}{\sqrt{a-b\cos\phi''}^n} \, \mathrm{d}\phi'' \tag{A.1}$$

Let us first find the solution of Equation (1) for $n=1$. For $n>1$, we can find the result by taking an integral of the solution for $n=1$ with respect to $-\lambda$. For instance we can obtain the solution for $n=2$,

$$\int_0^{2\pi} k_2 \cos^m \phi'' \frac{\mathrm{e}^{-\lambda\sqrt{a-b\cos\phi''}}}{\sqrt{a-b\cos\phi''}^2} \, \mathrm{d}\phi'' \tag{A.2}$$

by taking the integral of the solution for Equation (1) with respect to $-\lambda$ since Equation (2) is equal to the integral of Equation (1) with respect to $-\lambda$,

$$\int_0^{2\pi} k_2 \cos^m \phi'' \frac{\mathrm{e}^{-\lambda\sqrt{a-b\cos\phi''}}}{\sqrt{a-b\cos\phi''}^2} \, \mathrm{d}\phi'' = \int \mathrm{d}(-\lambda) \int_0^{2\pi} k_2 \cos^m \phi'' \frac{\mathrm{e}^{-\lambda\sqrt{a-b\cos\phi''}}}{\sqrt{a-b\cos\phi''}} \, \mathrm{d}\phi''$$

The integrals for other values of n can be found in a similar manner.

Let us represent $\sqrt{a - b\cos\phi''}^{\,n}$ in terms of a binomial function [26],

$$\sqrt{a - b\cos\phi''}^{\,n} = a^{n/2}\sum_{k=0}^{n/2}\left(-\frac{n}{2}\right)_k\left(\frac{b}{a\cos\phi''}\right)^k\frac{1}{k!} \quad \text{for } n \text{ even}$$

$$= a^{n/2}\sum_{k=0}^{\infty}\left(-\frac{n}{2}\right)_k\left(\frac{b}{a\cos\phi''}\right)^k\frac{1}{k!} \quad \text{for } n \text{ odd}$$

and let us represent the exponential in terms of its power series $\left(\mathrm{e}^{-x} = \sum_{j=0}^{\infty}(-x)^j/j!\right)$, and split the series to its even and odd functions,

$$\mathrm{e}^{-x} = \sum_{l=0}^{\infty}\frac{(-x)^{2l}}{(2l)!} + \sum_{l=0}^{\infty}\frac{(-x)^{2l+1}}{(2l+1)!}$$

We can therefore write Equation (1) as

$$\begin{aligned}\int_0^{2\pi}\mathrm{d}\phi''\cos^m\phi_p\frac{\mathrm{e}^{-\lambda\sqrt{a-b\cos\phi''}}}{\sqrt{a-b\cos\phi''}} = \int_0^{2\pi}\mathrm{d}\phi''&\left(\sum_{l=0}^{\infty}\frac{(-\lambda)^{2l}}{(2l)!}\sqrt{a}^{2l-1}\sum_{k=0}^{\infty}\left(\frac{-2l+1}{2}\right)_k\left(\frac{b}{a}\right)^k\right.\\ &\times\left(\frac{1}{\cos\phi''}\right)^{k-m}\frac{1}{k!} + \sum_{l=0}^{\infty}\frac{(-\lambda)^{2l+1}}{(2l+1)!}\sqrt{a}^{2l}\sum_{k=0}^{l}\left(\frac{-2l}{2}\right)_k\\ &\left.\times\left(\frac{b}{a}\right)^k\left(\frac{1}{\cos\phi''}\right)^{k-m}\frac{1}{k!}\right)\end{aligned} \qquad \text{(A.3)}$$

Using known Pochhammer identities, and recognizing modified Bessel Functions of the first kind $I_n(z)$ [26], we can write Equation (3) as

$$\begin{aligned}\int_0^{2\pi}\mathrm{d}\phi_p\cos^m\phi''\frac{\mathrm{e}^{-\lambda\sqrt{a-b\cos\phi''}}}{\sqrt{a-b\cos\phi''}} = \int_0^{2\pi}\mathrm{d}\phi''&\sum_{k=0,\text{even}}^{\infty}\left(\frac{b}{a}\right)^k\frac{(\cos\phi'')^{k-m}}{k!}\\ &\times\left(\left(\frac{1}{2}\right)_k\frac{1}{\sqrt{a}}\left(-\lambda\sqrt{a}\right)^{k+1/2}\Gamma\left(\frac{1}{2}-k\right)I_{-k-1/2}\left(-\lambda\sqrt{a}\right)\right)\\ &-\lambda(-1)^k\left(\frac{-\lambda\sqrt{a}}{2}\right)^{k-1/2}\Gamma\left(\frac{3}{2}\right)I_{k+1/2}\left(-\lambda\sqrt{a}\right)\end{aligned}$$

Since [27],

$$\int_0^{2\pi}(\cos\phi_p)^r = 4\cdot 2^{r-1}\mathrm{B}(r+1/2, r+1/2)$$

the integral can be expressed as

$$\begin{aligned}\int_0^{2\pi} \mathrm{d}\phi_p \cos^m \phi'' \frac{\mathrm{e}^{-\lambda\sqrt{a-b\cos\phi''}}}{\sqrt{a-b\cos\phi''}} &= \sum_{k=0,\text{even}}^{\infty} 4\cdot 2^{k-m-1}\mathrm{B}(k-m+1/2, k-m+1/2)\frac{1}{k!}\\ &\quad\times\left(\left(\frac{1}{2}\right)_k \frac{1}{\sqrt{a}}\left(-\lambda\sqrt{a}\right)^{k+1/2}\Gamma\left(\frac{1}{2}-k\right) I_{-k-1/2}\left(-\lambda\sqrt{a}\right)\right)\\ &\quad-\lambda(-1)^k\left(\frac{-\lambda\sqrt{a}}{2}\right)^{k-1/2}\Gamma\left(\frac{3}{2}\right) I_{k+1/2}\left(-\lambda\sqrt{a}\right)\end{aligned}$$

APPENDIX B: THE INTEGRATED TORQUE STOKESLET T′

The torque stokeslet T'_{uxi0} due to impulses in the x direction which are constant with respect to φ'; the two torque stokeslets which have the same weighting, T'_{uxi2} due to impulses in the x direction which vary as $\cos^2\varphi'$ and T'_{uyi} due to impulses in the y direction which vary as $\cos\varphi'\sin\varphi'$; and the torque stokeslets T'_{uzi} due to impulses in the z direction which vary as $\cos\varphi'$, are given in the following expressions:

$$\begin{aligned}
&T_{uxi0}\\
&= (-(2\pi\mu(-24c^3de+6cd^3e+6c^4f-24c^2d^2f-c^6f\lambda^2-2c^4d^2f\lambda^2-c^2d^4f\lambda^2-9cdec_0^2\\
&\quad+12c^2fc_0^2-6c^4f\lambda^2c_0^2-4c^2d^2f\lambda^2c_0^2+c^3f\lambda^2\cos[3\phi']c_0^3-3c^2f\lambda^2c_0^4+6c^3ed_z-24cd^2ed_z\\
&\quad+18c^2dfd_z-12d^3fd_z+c^5e\lambda^2d_z+2c^3d^2e\lambda^2d_z+cd^4e\lambda^2d_z+12cec_0^2d_z+18dfc_0^2d_z\\
&\quad+6c^3e\lambda^2c_0^2d_z+4cd^2e\lambda^2c_0^2d_z-c^2e\lambda^2\cos[3\phi']c_0^3d_z+3ce\lambda^2c_0^4d_z-c\cos[2\phi']c_0^2(15de-6cf\\
&\quad+4c^3f\lambda^2+2cd^2f\lambda^2+2cf\lambda^2c_0^2-6ed_z-4c^2e\lambda^2d_z-2d^2e\lambda^2d_z-2e\lambda^2c_0^2d_z)\\
&\quad+\cos[\phi']c_0(5c^5f\lambda^2+3c^3f(-6+2d^2\lambda^2+3\lambda^2c_0^2)-5c^4e\lambda^2d_z-e(-24d^2+d^4\lambda^2+6c_0^2\\
&\quad+2d^2\lambda^2c_0^2+\lambda^2c_0^4)d_z+cf(24d^2+d^4\lambda^2-6c_0^2+2d^2\lambda^2c_0^2+\lambda^2c_0^4-36dd_z)-3c^2e(-16d\\
&\quad+6d_z+2d^2\lambda^2d_z+3\lambda^2c_0^2d_z))))/(\lambda^2(a-b\cos[\phi'])^{7/2})+(2e^{-\lambda\sqrt{a-b\cos[\phi']}}\pi\mu(-24c^3de+6cd^3e\\
&\quad+6c^4f-24c^2d^2f-9c^5de\lambda^2-6c^3d^3e\lambda^2+3cd^5e\lambda^2+2c^6f\lambda^2-8c^4d^2f\lambda^2-10c^2d^4f\lambda^2\\
&\quad-24c^3de\lambda\sqrt{a-b\cos[\phi']}+6cd^3e\lambda\sqrt{a-b\cos[\phi']}+6c^4f\lambda\sqrt{a-b\cos[\phi']}-24c^2d^2f\lambda\\
&\quad\times\sqrt{a-b\cos[\phi']}-c^5de\lambda^3\sqrt{a-b\cos[\phi']}+cd^5e\lambda^3\sqrt{a-b\cos[\phi']}-2c^4d^2f\lambda^3\sqrt{a-b\cos[\phi']}\\
&\quad-2c^2d^4f\lambda^3\sqrt{a-b\cos[\phi']}-9cdec_0^2+12c^2fc_0^2-30c^3de\lambda^2c_0^2+12c^4f\lambda^2c_0^2-16c^2d^2f\lambda^2c_0^2\\
&\quad-9cde\lambda\sqrt{a-b\cos[\phi']}c_0^2+12c^2f\lambda\sqrt{a-b\cos[\phi']}c_0^2-3c^3de\lambda^3\sqrt{a-b\cos[\phi']}c_0^2+cd^3e\lambda^3\\
&\quad\times\sqrt{a-b\cos[\phi']}c_0^2-4c^2d^2f\lambda^3\sqrt{a-b\cos[\phi']}c_0^2+6c^2de\lambda^2\cos[3\phi']c_0^3-2c^3f\lambda^2\cos[3\phi']c_0^3
\end{aligned}$$

$$+c^2de\lambda^3\sqrt{a-b\cos[\phi']}\cos[3\phi']c_0^3-3cde\lambda^2c_0^4+6c^2f\lambda^2c_0^4+6c^3ed_z-24cd^2ed_z+18c^2dfd_z$$

$$-12d^3fd_z+c^5e\lambda^2d_z-10c^3d^2e\lambda^2d_z-11cd^4e\lambda^2d_z+6c^4df\lambda^2d_z-6d^5f\lambda^2d_z+6c^3e\lambda$$

$$\times\sqrt{a-b\cos[\phi']}d_z-24cd^2e\lambda\sqrt{a-b\cos[\phi']}d_z+18c^2df\lambda\sqrt{a-b\cos[\phi']}dz-12d^3f\lambda$$

$$\times\sqrt{a-b\cos[\phi']}dz-c^5e\lambda^3\sqrt{a-b\cos[\phi']}d_z-4c^3d^2e\lambda^3\sqrt{a-b\cos[\phi']}d_z-3cd^4e\lambda^3$$

$$\times\sqrt{a-b\cos[\phi']}d_z-2c^2d^3f\lambda^3\sqrt{a-b\cos[\phi']}d_z-2d^5f\lambda^3\sqrt{a-b\cos[\phi']}d_z+12cec_0^2d_z$$

$$+18dfc_0^2d_z+6c^3e\lambda^2c_0^2d_z-20cd^2e\lambda^2c_0^2d_z+24c^2df\lambda^2c_0^2d_z+12ce\lambda\sqrt{a-b\cos[\phi']}c_0^2d_z$$

$$+18df\lambda\sqrt{a-b\cos[\phi']}c_0^2d_z-6c^3e\lambda^3\sqrt{a-b\cos[\phi']}c_0^2d_z-8cd^2e\lambda^3\sqrt{a-b\cos[\phi']}c_0^2d_z$$

$$-2d^3f\lambda^3\sqrt{a-b\cos[\phi']}c_0^2d_z-c^2e\lambda^2\cos[3\phi']c_0^3d_z+c^2e\lambda^3\sqrt{a-b\cos[\phi']}\cos[3\phi']c_0^3d_z$$

$$+3ce\lambda^2c_0^4d_z+6df\lambda^2c_0^4d_z-3ce\lambda^3\sqrt{a-b\cos[\phi']}c_0^4d_z+c\cos[2\phi']c_0^2(-15de+6cf$$

$$-24c^2de\lambda^2-6d^3e\lambda^2+8c^3f\lambda^2-8cd^2f\lambda^2-15de\lambda\sqrt{a-b\cos[\phi']}+6cf\lambda\sqrt{a-b\cos[\phi']}$$

$$-3c^2de\lambda^3\sqrt{a-b\cos[\phi']}-d^3e\lambda^3\sqrt{a-b\cos[\phi']}-2cd^2f\lambda^3\sqrt{a-b\cos[\phi']}-6de\lambda^2c_0^2$$

$$+4cf\lambda^2c_0^2-de\lambda^3\sqrt{a-b\cos[\phi']}c_0^2+6ed_z+4c^2e\lambda^2d_z-10d^2e\lambda^2d_z+12cdf\lambda^2d_z+6e\lambda$$

$$\times\sqrt{a-b\cos[\phi']}d_z-4c^2e\lambda^3\sqrt{a-b\cos[\phi']}d_z-4d^2e\lambda^3\sqrt{a-b\cos[\phi']}d_z+2e\lambda^2c_0^2d_z-2e\lambda^3$$

$$\times\sqrt{a-b\cos[\phi']}c_0^2d_z)-\cos[\phi']c_0(10c^5f\lambda^2-e(24d^2+11d^4\lambda^2+24d^2\lambda\sqrt{a-b\cos[\phi']}$$

$$+3d^4\lambda^3\sqrt{a-b\cos[\phi']}-6c_0^2+10d^2\lambda^2c_0^2-6\lambda\sqrt{a-b\cos[\phi']}c_0^2+4d^2\lambda^3\sqrt{a-b\cos[\phi']}$$

$$c_0^2-\lambda^2c_0^4+\lambda^3\sqrt{a-b\cos[\phi']}c_0^4)d_z-6c^3f(-3+4d^2\lambda^2-3\lambda\sqrt{a-b\cos[\phi']}+d^2\lambda^3$$

$$\times\sqrt{a-b\cos[\phi']}-3\lambda^2c_0^2-4d\lambda^2d_z)-c^4e\lambda^2(36d+4d\lambda\sqrt{a-b\cos[\phi']}-5d_z+5\lambda$$

$$\times\sqrt{a-b\cos[\phi']}d_z)+2cf(-12d^2-5d^4\lambda^2-12d^2\lambda\sqrt{a-b\cos[\phi']}-d^4\lambda^3\sqrt{a-b\cos[\phi']}$$

$$+3c_0^2-4d^2\lambda^2c_0^2+3\lambda\sqrt{a-b\cos[\phi']}c_0^2-d^2\lambda^3\sqrt{a-b\cos[\phi']}c_0^2+\lambda^2c_0^4+18dd_z+18d\lambda$$

$$\times\sqrt{a-b\cos[\phi']}d_z-2d^3\lambda^3\sqrt{a-b\cos[\phi']}d_z+12d\lambda^2c_0^2d_z)-3c^2e(16d+4d^3\lambda^2+16d\lambda$$

$$\times\sqrt{a-b\cos[\phi']}+10d\lambda^2c_0^2+d\lambda^3\sqrt{a-b\cos[\phi']}c_0^2-6d_z+10d^2\lambda^2d_z-6\lambda\sqrt{a-b\cos[\phi']}d_z$$

$$+4d^2\lambda^3\sqrt{a-b\cos[\phi']}d_z-3\lambda^2c_0^2d_z+3\lambda^3\sqrt{a-b\cos[\phi']}c_0^2d_z))))/(\lambda^2(a-b\cos[\phi'])^{7/2})$$

$$\times h_1h_2h_1'h_2'$$

$$T_{uxi2}+T_{uyi}$$

$$=\frac{1}{\lambda^2(a-b\cos[\phi'])^{7/2}}(ce^{-\lambda\sqrt{a-b\ \cos[\phi']}}\pi(\cos[\phi']^2(12ade-60c^2de-12adee^{\lambda\sqrt{a-b\cos[\phi']}}$$

$$+60c^2dee^{\lambda\sqrt{a-b\cos[\phi']}}+12acf-60cd^2f-12ace^{\lambda\sqrt{a-b\cos[\phi']}}f+60cd^2e^{\lambda\sqrt{a-b\cos[\phi']}}f$$

$$+ 6a^2de\lambda^2 + 3b^2de\lambda^2 - 24ac^2de\lambda^2 + 4a^2cf\lambda^2 + 2b^2cf\lambda^2 - 24acd^2f\lambda^2 + 2a^2ce^{\lambda\sqrt{a-b\cos[\phi']}}f\lambda^2$$

$$+ b^2ce^{\lambda\sqrt{a-b\cos[\phi']}}f\lambda^2 + 12ade\lambda\sqrt{a-b\cos[\phi']} - 60c^2de\lambda\sqrt{a-b\cos[\phi']} + 12acf\lambda$$

$$\times\sqrt{a-b\cos[\phi']} - 60cd^2f\lambda\sqrt{a-b\cos[\phi']} + 2a^2de\lambda^3\sqrt{a-b\cos[\phi']} + b^2de\lambda^3\sqrt{a-b\cos[\phi']}$$

$$- 4ac^2de\lambda^3\sqrt{a-b\cos[\phi']} - 4acd^2f\lambda^3\sqrt{a-b\cos[\phi']} + 4b\cos[\phi'](cd^2f\lambda^2(6 + \lambda$$

$$\times\sqrt{a-b\cos[\phi']}) - cf(3 + 2a\lambda^2 + e^{\lambda\sqrt{a-b\cos[\phi']}}(-3 + a\lambda^2) + 3\lambda\sqrt{a-b\cos[\phi']}) + de(-3$$

$$+ 3e^{\lambda\sqrt{a-b\cos[\phi']}} + 6c^2\lambda^2 - 3\lambda\sqrt{a-b\cos[\phi']} + c^2\lambda^3\sqrt{a-b\cos[\phi']} - a\lambda^2(3 + \lambda$$

$$\times\sqrt{a-b\cos[\phi']}))) + b^2\lambda^2(c(2 + e^{\lambda\sqrt{a-b\cos[\phi']}})f + de(3 + \lambda\sqrt{a-b\cos[\phi']}))\cos[2\phi'])$$

$$- \cos[\phi'](-90cde + 90cdee^{\lambda\sqrt{a-b\cos[\phi']}} + 12af - 60d^2f - 12ae^{\lambda\sqrt{a-b\cos[\phi']}}f$$

$$+ 60d^2e^{\lambda\sqrt{a-b\cos[\phi']}}f - 36acde\lambda^2 + 4a^2f\lambda^2 + 2b^2f\lambda^2 - 24ad^2f\lambda^2 + 2a^2e^{\lambda\sqrt{a-b\cos[\phi']}}f\lambda^2$$

$$+ b^2e^{\lambda\sqrt{a-b\cos[\phi']}}f\lambda^2 - 90cde\lambda\sqrt{a-b\cos[\phi']} + 12af\lambda\sqrt{a-b\cos[\phi']} - 60d^2f\lambda$$

$$\times\sqrt{a-b\cos[\phi']} - 6acde\lambda^3\sqrt{a-b\cos[\phi']} - 4ad^2f\lambda^3\sqrt{a-b\cos[\phi']} - b\cos[\phi'](-7cde\lambda^2(6$$

$$+ \lambda\sqrt{a-b\cos[\phi']}) + 4f(3 + 2a\lambda^2 - 6d^2\lambda^2 + e^{\lambda\sqrt{a-b\cos[\phi']}}(-3 + a\lambda^2) + 3\lambda$$

$$\times\sqrt{a-b\cos[\phi']} - d^2\lambda^3\sqrt{a-b\cos[\phi']})) + (b^2(2 + e^{\lambda\sqrt{a-b\cos[\phi']}})f\lambda^2 + 2cde(15e^{\lambda\sqrt{a-b\cos[\phi']}}$$

$$-15(1 + \lambda\sqrt{a-b\cos[\phi']}) - a\lambda^2(6 + \lambda\sqrt{a-b\cos[\phi']})))\cos[2\phi'] + 6bcde\lambda^2\cos[3\phi']$$

$$+ bcde\lambda^3\sqrt{a-b\cos[\phi']}\cos[3\phi'])c_0 + 4de\cos[\phi']^2(-15 + 15e^{\lambda\sqrt{a-b\cos[\phi']}} - 6a\lambda^2 - 15\lambda$$

$$\times\sqrt{a-b\cos[\phi']} - a\lambda^3\sqrt{a-b\cos[\phi']} + b\lambda^2\cos[\phi'](6 + \lambda\sqrt{a-b\cos[\phi']}))c_0^2 - a^2e$$

$$\times e^{\lambda\sqrt{a-b\cos[\phi']}}\lambda^2 d_z)h_1h_2h'_1h'_2)$$

$$- \frac{1}{4\lambda^2(a-b\cos[\phi'])^{7/2}}(e^{-\lambda\sqrt{a-b\cos[\phi']}}\pi(96ace - 120c^3e - 96acee^{\lambda\sqrt{a-b\cos[\phi']}}$$

$$+ 120c^3ee^{\lambda\sqrt{a-b\cos[\phi']}} + 48adf - 120c^2df - 48ade^{\lambda\sqrt{a-b\cos[\phi']}}f + 120c^2de^{\lambda\sqrt{a-b\cos[\phi']}}f$$

$$+ 44a^2ce\lambda^2 + 27b^2ce\lambda^2 - 48ac^3e\lambda^2 + 3b^2cee^{\lambda\sqrt{a-b\cos[\phi']}}\lambda^2 + 24a^2df\lambda^2 + 12b^2df\lambda^2$$

$$- 48ac^2df\lambda^2 + 96ace\lambda\sqrt{a-b\cos[\phi']} - 120c^3e\lambda\sqrt{a-b\cos[\phi']} + 48adf\lambda\sqrt{a-b\cos[\phi']}$$

$$- 120c^2df\lambda\sqrt{a-b\cos[\phi']} + 12a^2ce\lambda^3\sqrt{a-b\cos[\phi']} + 7b^2ce\lambda^3\sqrt{a-b\cos[\phi']} - 8ac^3e\lambda^3$$

$$\times\sqrt{a-b\cos[\phi']} + 8a^2df\lambda^3\sqrt{a-b\cos[\phi']} + 4b^2df\lambda^3\sqrt{a-b\cos[\phi']} - 8ac^2df\lambda^3$$

$$\times\sqrt{a-b\cos[\phi']} + 4b\cos[\phi'](3c^3e\lambda^2(6 + \lambda\sqrt{a-b\cos[\phi']}) + 3c^2df\lambda^2(6 + \lambda\sqrt{a-b\cos[\phi']})$$

$$+ 4df(3e^{\lambda\sqrt{a-b\cos[\phi']}} - 3(1 + \lambda\sqrt{a-b\cos[\phi']}) - a\lambda^2(3 + \lambda\sqrt{a-b\cos[\phi']}))$$

$$- ce(3e^{\lambda\sqrt{a-b\cos[\phi']}}(-10 + a\lambda^2) + 30(1 + \lambda\sqrt{a-b\cos[\phi']}) + a\lambda^2(27 + 7\lambda\sqrt{a-b\cos[\phi']})))$$

$$+48ace\cos[2\phi'] - 120c^3e\cos[2\phi'] - 48acee^{\lambda\sqrt{a-b\cos[\phi']}}\cos[2\phi'] + 120c^3ee^{\lambda\sqrt{a-b\cos[\phi']}}$$

$$\times\cos[2\phi'] - 120c^2df\cos[2\phi'] + 120c^2de^{\lambda\sqrt{a-b\cos[\phi']}}f\cos[2\phi'] + 20a^2ce\lambda^2\cos[2\phi']$$

$$+32b^2ce\lambda^2\cos[2\phi'] - 48ac^3e\lambda^2\cos[2\phi'] + 4a^2cee^{\lambda\sqrt{a-b\cos[\phi']}}\lambda^2\cos[2\phi'] + 4b^2ce$$

$$\times e^{\lambda\sqrt{a-b\cos[\phi']}}\lambda^2\cos[2\phi'] + 12b^2df\lambda^2\cos[2\phi'] - 48ac^2df\lambda^2\cos[2\phi'] + 48ace\lambda\sqrt{a-b\cos[\phi']}$$

$$\times\cos[2\phi'] - 120c^3e\lambda\sqrt{a-b\cos[\phi']}\cos[2\phi'] - 120c^2df\lambda\sqrt{a-b\cos[\phi']}\cos[2\phi'] + 4a^2ce\lambda^3$$

$$\times\sqrt{a-b\cos[\phi']}\cos[2\phi'] + 8b^2ce\lambda^3\sqrt{a-b\cos[\phi']}\cos[2\phi'] - 8ac^3e\lambda^3\sqrt{a-b\cos[\phi']}\cos[2\phi']$$

$$+4b^2df\lambda^3\sqrt{a-b\cos[\phi']}\cos[2\phi'] - 8ac^2df\lambda^3\sqrt{a-b\cos[\phi']}\cos[2\phi'] - 24bce\cos[3\phi']$$

$$+24bcee^{\lambda\sqrt{a-b\cos[\phi']}}\cos[3\phi'] - 20abce\lambda^2\cos[3\phi'] + 24bc^3e\lambda^2\cos[3\phi'] - 4abcee^{\lambda\sqrt{a-b\cos[\phi']}}$$

$$\times\lambda^2\cos[3\phi'] + 24bc^2df\lambda^2\cos[3\phi'] - 24bce\lambda\sqrt{a-b\cos[\phi']}\cos[3\phi'] - 4abce\lambda^3\sqrt{a-b\cos[\phi']}$$

$$\times\cos[3\phi'] + 4bc^3e\lambda^3\sqrt{a-b\cos[\phi']}\cos[3\phi'] + 4bc^2df\lambda^3\sqrt{a-b\cos[\phi']}\cos[3\phi'] + 5b^2ce\lambda^2$$

$$\times\cos[4\phi'] + b^2cee^{\lambda\sqrt{a-b\cos[\phi']}}\lambda^2\cos[4\phi'] + b^2ce\lambda^3\sqrt{a-b\cos[\phi']}\cos[4\phi'] - 4\cos[\phi'](36ae$$

$$-150c^2e - 36aee^{\lambda\sqrt{a-b\cos[\phi']}} + 150c^2ee^{\lambda\sqrt{a-b\cos[\phi']}} - 120cdf + 120cde^{\lambda\sqrt{a-b\cos[\phi']}}f$$

$$+16a^2e\lambda^2 + 8b^2e\lambda^2 - 60ac^2e\lambda^2 + 2a^2ee^{\lambda\sqrt{a-b\cos[\phi']}}\lambda^2 + b^2ee^{\lambda\sqrt{a-b\cos[\phi']}}\lambda^2 - 48acdf\lambda^2$$

$$+36ae\lambda\sqrt{a-b\cos[\phi']} - 150c^2e\lambda\sqrt{a-b\cos[\phi']} - 120cdf\lambda\sqrt{a-b\cos[\phi']} + 4a^2e\lambda^3$$

$$\times\sqrt{a-b\cos[\phi']} + 2b^2e\lambda^3\sqrt{a-b\cos[\phi']} - 10ac^2e\lambda^3\sqrt{a-b\cos[\phi']} - 8acdf\lambda^3$$

$$\times\sqrt{a-b\cos[\phi']} - b\cos[\phi'](-8cdf\lambda^2(6+\lambda\sqrt{a-b\cos[\phi']}) + e(36 - 66c^2\lambda^2$$

$$+4e^{\lambda\sqrt{a-b\cos[\phi']}}(-9+a\lambda^2) + 36\lambda\sqrt{a-b\cos[\phi']} - 11c^2\lambda^3\sqrt{a-b\cos[\phi']}$$

$$+8a\lambda^2(4+\lambda\sqrt{a-b\cos[\phi']}))) + e(b^2\lambda^2(8 + e^{\lambda\sqrt{a-b\cos[\phi']}} + 2\lambda\sqrt{a-b\cos[\phi']})$$

$$+2c^2(15e^{\lambda\sqrt{a-b\cos[\phi']}} - 15(1+\lambda\sqrt{a-b\cos[\phi']}) - a\lambda^2(6+\lambda\sqrt{a-b\cos[\phi']})))$$

$$\times\cos[2\phi'] + 6bc^2e\lambda^2\cos[3\phi'] + bc^2e\lambda^3\sqrt{a-b\cos[\phi']}\cos[3\phi'])c_0$$

$$+16(-15 + 15e^{\lambda\sqrt{a-b\cos[\phi']}} - 6a\lambda^2 - 15\lambda\sqrt{a-b\cos[\phi']} - a\lambda^3\sqrt{a-b\cos[\phi']} + b\lambda^2$$

$$\times\cos[\phi'](6+\lambda\sqrt{a-b\cos[\phi']}))(2ce + df + ce\cos[2\phi'])c_0^2 - 16e\cos[\phi'](-15$$

$$+15e^{\lambda\sqrt{a-b\cos[\phi']}} - 6a\lambda^2 - 15\lambda\sqrt{a-b\cos[\phi']} - a\lambda^3\sqrt{a-b\cos[\phi']} + b\lambda^2\cos[\phi'](6+\lambda$$

$$\times\sqrt{a-b\cos[\phi']}))c_0^3)d_zh_1h_2h_1'h_2')$$

T_{uzi}

$$= \frac{1}{\lambda^2(a-b\cos[\phi'])^{7/2}}(e^{-\lambda\sqrt{a-b\cos[\phi']}}\pi(-b^2ce\lambda^2\cos[\phi']^4(3+\lambda\sqrt{a-b\cos[\phi']})c_0$$

$$+ 2b\cos[\phi']^3(bc^2e\lambda^2(3 + \lambda\sqrt{a - b\cos[\phi']}) - bde(2 + e^{\lambda\sqrt{a-b\cos[\phi']}})\lambda^2d_z + c(-ec_0(-3$$

$$+ 3e^{\lambda\sqrt{a-b\cos[\phi']}} + 6d^2\lambda^2 - 3\lambda\sqrt{a - b\cos[\phi']} + d^2\lambda^3\sqrt{a - b\cos[\phi']} - a\lambda^2(3 + \lambda$$

$$\times \sqrt{a - b\cos[\phi']}) - 6d\lambda^2d_z - d\lambda^3\sqrt{a - b\cos[\phi']}d_z) + bf\lambda^2(d(8 + e^{\lambda\sqrt{a-b\cos[\phi']}}$$

$$+ 2\lambda\sqrt{a - b\cos[\phi']}) - (3 + \lambda\sqrt{a - b\cos[\phi']})d_z))) + c_0(-a^2\lambda^2(3 + \lambda\sqrt{a - b\cos[\phi']})$$

$$\times (ce - 2fd_z) - 30d(-1 + e^{\lambda\sqrt{a-b\cos[\phi']}} - \lambda\sqrt{a - b\cos[\phi']})(ce(d - 3d_z) - 2dfd_z)$$

$$+ 2a(-2f(3e^{\lambda\sqrt{a-b\cos[\phi']}} - 3(1 + \lambda\sqrt{a - b\cos[\phi']}) + d^2\lambda^2(6 + \lambda\sqrt{a - b\cos[\phi']}))d_z)$$

$$+ ce(3e^{\lambda\sqrt{a-b\cos[\phi']}} - 3(1 + \lambda\sqrt{a - b\cos[\phi']}) + d^2\lambda^2(6 + \lambda\sqrt{a - b\cos[\phi']}) - 3d\lambda^2(6$$

$$+ \lambda\sqrt{a - b\cos[\phi']}d_z)) + ce\sin[\phi']^2(a^2\lambda^2(3 + \lambda\sqrt{a - b\cos[\phi']}) + 30d(-1$$

$$+ e^{\lambda\sqrt{a-b\cos[\phi']}} - \lambda\sqrt{a - b\cos[\phi']})(d - d_z) - 2a(3e^{\lambda\sqrt{a-b\cos[\phi']}}) - 3(1 + \lambda\sqrt{a - b\cos[\phi']}$$

$$+ d^2\lambda^2(6 + \lambda\sqrt{a - b\cos[\phi']}) - d\lambda^2(6 + \lambda\sqrt{a - b\cos[\phi']}d_z))) + 2\cos[\phi'](-30c^2d^2e$$

$$+ 30c^2d^2ee^{\lambda\sqrt{a-b\cos[\phi']}} - 30cd^3f + 30cd^3e^{\lambda\sqrt{a-b\cos[\phi']}}f - 30c^2d^2e\lambda\sqrt{a - b\cos[\phi']}$$

$$- 30cd^3f\lambda\sqrt{a - b\cos[\phi']} + 3bcec_0 - 3bcee^{\lambda\sqrt{a-b\cos[\phi']}}c_0 - 6bcd^2e\lambda^2c_0 + 3bce\lambda$$

$$\times \sqrt{a - b\cos[\phi']}c_0 - bcd^2e\lambda^3\sqrt{a - b\cos[\phi']}c_0 + 30c^2ded_z - 30c^2dee^{\lambda\sqrt{a-b\cos[\phi']}}d_z$$

$$+ 30cd^2fd_z - 30cd^2e^{\lambda\sqrt{a-b\cos[\phi']}}fd_z + 30c^2de\lambda\sqrt{a - b\cos[\phi']}d_z + 30cd^2f\lambda$$

$$\times \sqrt{a - b\cos[\phi']}d_z - 6bfc_0d_z + 6be^{\lambda\sqrt{a-b\cos[\phi']}}fc_0d_z + 18bcde\lambda^2c_0d_z + 12bd^2f\lambda^2c_0d_z$$

$$- 6bf\lambda\sqrt{a - b\cos[\phi']}c_0d_z + 3bcdde\lambda^3\sqrt{a - b\cos[\phi']}c_0d_z + 2bd^2f\lambda^3\sqrt{a - b\cos[\phi']}$$

$$\times c_0d_z + 30dec_0^2d_z - 30dee^{\lambda\sqrt{a-b\cos[\phi']}}c_0^2d_z + 30de\lambda\sqrt{a - b\cos[\phi']}c_0^2d_z + bce\sin[\phi']^2c_0(-3$$

$$+ 3e^{\lambda\sqrt{a-b\cos[\phi']}} + 6d^2\lambda^2 - 3\lambda\sqrt{a - b\cos[\phi']} + d^2\lambda^3\sqrt{a - b\cos[\phi']} - a\lambda^2(3 + \lambda$$

$$\times \sqrt{a - b\cos[\phi']}) - 6d\lambda^2d_z - d\lambda^3\sqrt{a - b\cos[\phi']}d_z) + a^2\lambda^2(c^2e(3 + \lambda\sqrt{a - b\cos[\phi']})$$

$$- de(2 + e^{\lambda\sqrt{a-b\cos[\phi']}})d_z + cf(d(8 + e^{\lambda\sqrt{a-b\cos[\phi']}} + 2\lambda\sqrt{a - b\cos[\phi']}) - (3 + \lambda$$

$$\times \sqrt{a - b\cos[\phi']})d_z)) + a(2(-bf\lambda^2(3 + \lambda\sqrt{a - b\cos[\phi']})c_0 + de(3e^{\lambda\sqrt{a-b\cos[\phi']}} - 3(1$$

$$+ \lambda\sqrt{a - b\cos[\phi']}) + \lambda^2(6 + \lambda\sqrt{a - b\cos[\phi']})c_0^2))d_z - 2c^2e(3e^{\lambda\sqrt{a-b\cos[\phi']}} - 3(1$$

$$+ \lambda\sqrt{a - b\cos[\phi']}) + d^2\lambda^2(6 + \lambda\sqrt{a - b\cos[\phi']} - d\lambda^2(6 + \lambda\sqrt{a - b\cos[\phi']})d_z)$$

$$+ c(-18df(-1 + e^{\lambda\sqrt{a-b\cos[\phi']}} - \lambda\sqrt{a - b\cos[\phi']}) - 2d^3f\lambda^2(6 + \lambda\sqrt{a - b\cos[\phi']})$$

$$+ be\lambda^2(3 + \lambda\sqrt{a - b\cos[\phi']})c_0 + 6f(-1 + e^{\lambda\sqrt{a-b\cos[\phi']}} - \lambda\sqrt{a - b\cos[\phi']})d_z$$

$$+ 2d^2f\lambda^2(6 + \lambda\sqrt{a - b\cos[\phi']})d_z))) + \cos[\phi']^2(b^2ce\lambda^2(3 + \lambda\sqrt{a - b\cos[\phi']})\sin[\phi']^2c_0$$

$$- b^2\lambda^2(3 + \lambda\sqrt{a - b\cos[\phi']})c_0(ce - 2fd_z) - cec_0(a^2\lambda^2(3 + \lambda\sqrt{a - b\cos[\phi']}) + 30d(-1$$

$$
\begin{aligned}
&+e^{\lambda\sqrt{a-b\cos[\phi']}}-\lambda\sqrt{a-b\cos[\phi']})(d-d_z)-2a(3e^{\lambda\sqrt{a-b\cos[\phi']}}-3(1+\lambda\sqrt{a-b\cos[\phi']})\\
&+d^2\lambda^2(6+\lambda\sqrt{a-b\cos[\phi']})-d\lambda^2(6+\lambda\sqrt{a-b\cos[\phi']})d_z))+4b(de(3+2a\lambda^2\\
&+e^{\lambda\sqrt{a-b\cos[\phi']}}(-3+a\lambda^2)+3\lambda\sqrt{a-b\cos[\phi']}-6\lambda^2c_0^2-\lambda^3\sqrt{a-b\cos[\phi']}c_0^2)d_z+c^2\\
&\times e(-3+3e^{\lambda\sqrt{a-b\cos[\phi']}}+6d^2\lambda^2-3\lambda\sqrt{a-b\cos[\phi']}+d^2\lambda^3\sqrt{a-b\cos[\phi']}-a\lambda^2(3+\lambda\\
&\times\sqrt{a-b\cos[\phi']})-6d\lambda^2d_z-d\lambda^3\sqrt{a-b\cos[\phi']}d_z)+cf(d^3\lambda^2(6+\lambda\sqrt{a-b\cos[\phi']})\\
&-d(9+e^{\lambda\sqrt{a-b\cos[\phi']}}(-9+a\lambda^2)+9\lambda\sqrt{a-b\cos[\phi']}+2a\lambda^2(4+\lambda\sqrt{a-b\cos[\phi']}))\\
&-d^2\lambda^2(6+\lambda\sqrt{a-b\cos[\phi']})d_z+(3-3e^{\lambda\sqrt{a-b\cos[\phi']}}+3\lambda\sqrt{a-b\cos[\phi']}+a\lambda^2(3\\
&+\lambda\sqrt{a-b\cos[\phi']}))d_z))))h_1h_2h_1'h_2')
\end{aligned}
$$

where

$$
\begin{aligned}
a&=-2L^2\cos[\eta]\cos[\eta']\cosh[\xi]\cosh[\xi']+L^2(\cos[\eta]^2+\sinh[\xi]^2)\\
&\quad+L^2(\cos[\eta']^2+\sinh[\xi']^2)\\
b&=2L^2\sin[\eta]\sin[\eta']\sinh[\xi]\sinh[\xi']\\
c&=L\sin[\eta]\sinh[\xi]\\
c_0&=L\sin[\eta']\sinh[\xi']\\
d&=L\cos[\eta]\cosh[\xi]-L\cos[\eta']\cosh[\xi']\\
d_z&=L\cos[\eta]\cosh[\xi]\\
e&=\frac{\sqrt{2}\cosh[\xi]\sin[\eta]}{\sqrt{-\cos[2\eta]+\cosh[2\xi]}}\\
f&=\frac{\sqrt{2}\cos[\eta]\sinh[\xi]}{\sqrt{-\cos[2\eta]+\cosh[2\xi]}}\\
h_1&=L\sin[\eta]\sinh[\xi]\\
h_2&=L\sqrt{\sin[\eta]^2+\sinh[\xi]^2}\\
h_1'&=L\sin[\eta']\sinh[\xi']\\
h_2'&=L\sqrt{\sin[\eta']^2+\sinh[\xi']^2}
\end{aligned}
$$

ACKNOWLEDGEMENTS

The author wishes to thank the National Science Foundation, Michael Shatz, and Steve Colburn for their support.

REFERENCES

1. Freeman DM, Weiss TF. On the role of fluid inertia and viscosity in stereociliary tuft motion: Analysis of isolated bodies of regular geometry. In *Lecture Notes in Biomathematics-Peripheral Auditory Mechanisms*, Allen JB *et al*. (eds), vol. 64. Springer: New York, 1986; 147–154.
2. Hyman WA. Shear flow over a protrusion from a plane wall. *Journal of Biomechanics* 1972; **5**:45–48 (Corrigendum on page 643).
3. Price TC. Slow linear shear flow past a hemispheroidal bump in a plane wall. *Quarterly Journal of Mechanics and Applied Mathematics* 1985; **38**:93–104.
4. Shatz L. Indirect boundary element method for shear flow over prolate and oblate hemispheroidal protuberances on plane walls. *International Journal for Numerical Methods in Fluids* 1998; **28**:961–981.
5. Chwang AT, Wu TY. Hydromechanics of low-Reynolds-number flow. Part 2. Singularity method for Stokes flows. *Journal of Fluid Mechanics* 1975; **67**:787–815.
6. Pozrikidis C. A study of linearized oscillatory flow past particles by the boundary integral method. *Journal of Fluid Mechanics* 1989; **202**:17–41.
7. Lewis ER, Leverenz EL, Bialek WS. *The Vertebrate Inner Ear*. CRC Press: Boca Raton, FL, 1985.
8. Freeman DM, Weiss TF. Hydrodynamic analysis of a two-dimensional model for micromechanical resonance of free-standing hair bundles. *Hearing Research* 1990; **48**:37–68.
9. Shatz L. The effect of hair bundle shape on hair bundle hydrodynamics of sensory cells in the inner ear. Thesis: Electrical and Computer Engineering. Massachusetts Institute of Technology: Cambridge, MA, 1996.
10. Shatz L. The effect of hair bundle shape on hair bundle hydrodynamics of inner ear hair cells at low and high frequencies. *Hearing Research* 2000; **141**:39–50.
11. Shatz L. The effect of shape on the hydrodynamics of a hemispheroid projecting from a plate in irrotational fluid. *Physics of Fluids* 1998; **10**:2177–2187.
12. Freeman DM, Weiss TF. Superposition of hydrodynamic forces on a hair bundle. *Hearing Research* 1990; **48**:1–16.
13. Freeman DM, Weiss TF. Hydrodynamic forces on hair bundles at low frequencies. *Hearing Research* 1990; **48**:17–30.
14. Freeman DM, Weiss TF. Hydrodynamic forces on hair bundles at high frequencies. *Hearing Research* 1990; **48**:31–36.
15. Landau LD, Lifshitz EM. *Fluid Mechanics*. Pergamon Press: Elmsford, NY, 1959.
16. Lamb H. *Hydrodynamics* (6th edn). Dover Publications: New York, 1945; 138–142.
17. Moon P, Spencer DE. *Field Theory Handbook* (2nd edn). Springer: Berlin, 1971; 28–33.
18. Pozrikidis C. Shear flow over a protuberance on a plane wall. *Journal of Engineering Mathematics* 1997; **31**:29–42.
19. Shatz L. Singularity method for oblate and prolate spheroids in Stokes and linearized oscillatory flow, in preparation.
20. Chwang AT, Wu TY. A note of potential flow involving prolate spheroids. *Schiffstechnik* 1974; **21**:19–30.
21. Batchelor GK. *An Introduction to Fluid Dynamics*. Cambridge University Press: Cambridge, 1967; 380,452.
22. Dean WR. Note on the slow motion of fluid. *Proceedings of the Cambridge Philosophical Society* 1936; **32**:598–613.
23. Wolfram S. *Mathematica*. Wolfram Research: Champaign, 2002.
24. Aranyosi AJ. *Measuring Sound-Induced Motions of the Alligator Lizard Cochlea*. Massachusetts Institute of Technology: Cambridge, MA, 2002.
25. Mulroy MJ, Williams RS. Auditory stereocilia in the alligator lizard. *Hearing Research* 1987; **25**:11–21.
26. Slater L. *Generalized Hypergeometric Functions*. Cambridge University Press: London, 1996.
27. Gradshteyn I, Ryzhik I. In *Table of Integrals*, *Series*, *and Products*, Jeffrey A (ed). Academic Press: New York, 1994.